



THE DOUBLE-PEAKED SN 2013ge: A TYPE Ib/c SN WITH AN ASYMMETRIC MASS EJECTION OR AN EXTENDED PROGENITOR ENVELOPE

M. R. DROUT¹, D. MILISAVLJEVIC¹, J. PARRENT¹, R. MARGUTTI¹, A. KAMBLE¹, A. M. SODERBERG¹, P. CHALLIS¹, R. CHORNOCK², W. FONG^{3,13}, S. FRANK⁴, N. GEHRELS⁵, M. L. GRAHAM⁶, E. HSIAO^{7,8}, K. ITAGAKI⁹, M. KASLIWAL¹⁰, R. P. KIRSHNER¹, D. MACOMB¹¹, G. H. MARION¹², J. NORRIS¹¹, AND M. M. PHILLIPS⁸

¹ Harvard-Smithsonian Center for Astrophysics, 60 Garden Street, Cambridge, MA 02138, USA; mdrout@cfa.harvard.edu

² Astrophysical Institute, Department of Physics and Astronomy, 251B Clipping Lab, Ohio University, Athens, OH 45701, USA

³ Steward Observatory, University of Arizona, 933 North Cherry Avenue, Tucson, AZ 85721, USA

⁴ Department of Astronomy, The Ohio State University, 140 West 18th Avenue, Columbus, OH 43210, USA

⁵ NASA Goddard Space Flight Center, Greenbelt, MD 20771, USA

⁶ Department of Astronomy, University of California, Berkeley, CA 94720-3411, USA

⁷ Department of Physics and Astronomy, Aarhus University, Ny Munkegade 120, DK-8000 Aarhus C, Denmark

⁸ Carnegie Observatories, Las Campanas Observatory, Colina El Pino, Casilla 601, Chile

⁹ Itagaki Astronomical Observatory, Teppo-cho, Yamagata, Yamagata 990-2492, Japan

¹⁰ Observatories of the Carnegie Institution for Science, 813 Santa Barbara Street, Pasadena, CA 91101, USA

¹¹ Boise State University, Department of Physics, 1910 University Drive, Boise, ID 83725 USA

¹² Department of Astronomy, University of Texas at Austin, Austin, TX 78712, USA

Received 2015 June 29; accepted 2016 February 23; published 2016 April 11

ABSTRACT

We present extensive multiwavelength (radio to X-ray) observations of the Type Ib/c supernova (SN Ib/c) SN 2013ge from -13 to $+457$ days relative to maximum light, including a series of optical spectra and *Swift* UV–optical photometry beginning 2–4 days post-explosion. This data set makes SN 2013ge one of the best-observed normal SNe Ib/c at early times—when the light curve is particularly sensitive to the progenitor configuration and mixing of radioactive elements—and reveals two distinct light curve components in the UV bands. The first component rises over 4–5 days and is visible for the first week post-explosion. Spectra of the first component have blue continua and show a plethora of moderately high velocity ($\sim 15,000 \text{ km s}^{-1}$) but narrow ($\sim 3500 \text{ km s}^{-1}$) spectroscopic features, indicating that the line-forming region is restricted. The explosion parameters estimated for the bulk explosion ($M_{\text{ej}} \sim 2\text{--}3 M_{\odot}$; $E_K \sim (1\text{--}2) \times 10^{51} \text{ erg}$) are standard for SNe Ib/c, and there is evidence for *weak* He features at early times—in an object that would have otherwise been classified as Type Ic. In addition, SN 2013ge exploded in a low-metallicity environment ($\sim 0.5 Z_{\odot}$), and we have obtained some of the deepest radio and X-ray limits for an SN Ib/c to date, which constrain the progenitor mass-loss rate to be $\dot{M} < 4 \times 10^{-6} M_{\odot} \text{ yr}^{-1}$. We are left with two distinct progenitor scenarios for SN 2013ge, depending on our interpretation of the early emission. If the first component is cooling envelope emission, then the progenitor of SN 2013ge either possessed an extended ($\gtrsim 30 R_{\odot}$) envelope or ejected a portion of its envelope in the final $\lesssim 1$ yr before core collapse. Alternatively, if the first component is due to outwardly mixed ^{56}Ni , then our observations are consistent with the asymmetric ejection of a distinct clump of nickel-rich material at high velocities. Current models for the collision of an SN shock with a binary companion cannot reproduce both the timescale and luminosity of the early emission in SN 2013ge. Finally, the spectra of the first component of SN 2013ge are similar to those of the rapidly declining SN 2002bj.

Key words: supernovae: general – supernovae: individual (SN 2013ge)

1. INTRODUCTION

Type Ib/c supernovae (SNe Ib/c) are an observational subclass of stellar explosions. They are identified mainly by a lack of either strong hydrogen or strong silicon features in their optical spectra (see Wheeler et al. 1995; Filippenko 1997 for a review of SN classifications). This class can be further divided into SNe Ib, which show conspicuous lines of helium in their spectra, and SNe Ic, which do not. These events are physically understood to be the core collapse of massive stars that were stripped of their hydrogen envelopes. Main progenitor channels include isolated Wolf-Rayet (W-R) stars with massive winds (Begelman & Sarazin 1986; Woosley & Weaver 1995) and lower-mass helium stars stripped by binary companions (Wheeler & Levreault 1985; Podsiadlowski et al. 1992; Yoon et al. 2010).

Two of the main power sources that contribute to the rising phase of an SN light curve are the radioactive decay of ^{56}Ni synthesized in the explosion and the cooling envelope emission produced when the ejecta radiates away energy deposited by the SN shock (e.g., Piro & Nakar 2013). In stripped-envelope SNe, ^{56}Ni powers a majority of the light curve, while cooling envelope emission is only predicted to be visible for a few days post-explosion. As a result, early observations of SNe Ib/c provide a particularly sensitive probe of both the structure of the progenitor star prior to explosion (Nakar & Sari 2010; Rabinak & Waxman 2011; Nakar & Piro 2014) and the degree to which radioactive materials are mixed into the outer ejecta (Dessart et al. 2012; Piro & Nakar 2013).

Constraints on the structure of the progenitor star from cooling envelope emission are valuable, as the final radii of putative Type Ib/c progenitors are predicted to vary by an order of magnitude or more depending on their initial conditions (mass, metallicity) and evolutionary history (single

¹³ Einstein Fellow.

versus binary) (Yoon et al. 2010). While no cooling envelope emission has been observed for a normal (not broad-lined) SN Ic to date, nondetections have been used to place constraints on the progenitor radii in several objects (e.g., PTF10vgv; Corsi et al. 2012). In addition, when interpreted as shock breakout emission, the early X-ray/UV peak observed from the Type Ib SN 2008D constrains its progenitor radius to be $\lesssim 12 R_{\odot}$ (Soderberg et al. 2008; but see also, e.g., Mazzali et al. 2008; Bersten et al. 2013, for alternative interpretations of this emission).

In addition, recent observations have highlighted gaps in our understanding of the final state of the progenitors for some SNe. For example, a handful of SNe with double-peaked optical light curves have been discovered. When interpreted as cooling envelope emission, the first peak requires that the progenitor star possessed a low-mass extended envelope, which differs from the standard hydrostatic models of stellar structure (Bersten et al. 2012; Nakar & Piro 2014; Nakar 2015). While a majority of these events are of Type IIb (e.g., SN 1993J, Wheeler et al. 1993; SN 2011dh, Arcavi et al. 2011; SN 2013df, Van Dyk et al. 2014), a similar morphology has also been observed in the Type Ibn iPTF 13beo (Gorbikov et al. 2014) and the Ic-BL SN 2006aj associated with gamma-ray burst (GRB) 060218 (Campana et al. 2006; Nakar 2015). Further, X-ray observations point to a subset of long GRB progenitors that either underwent enhanced mass loss in the final years before explosion or possess low-mass, extended, progenitor envelopes (Margutti et al. 2015).

Constraints on the mixing of radioactive material from rising light curves can also provide insight into the progenitor structure and explosion mechanism for various subclasses of SNe Ib/c. Mixing in core-collapse SNe can be accomplished by a number of mechanisms, including a large-scale asymmetry of the explosion (e.g., a “jet”-like explosion), a large-scale asymmetry of the SN shock produced by the neutrino or magnetorotational mechanism (e.g., Maeda et al. 2002; Scheck et al. 2006; Burrows et al. 2007; Marek & Janka 2009), and smaller-scale Rayleigh–Taylor and Kelvin–Helmholtz instabilities at the shock front (Kifonidis et al. 2006; Joggerst et al. 2009; Hammer et al. 2010). The observed signature of such mixing will vary depending on its origin, ranging from small modifications to the timescale and colors on the rise for well-mixed shallow deposits of ^{56}Ni (Dessart et al. 2012) to double-peaked light curves for asymmetric ejections of material. Models of the latter type have been investigated as a possible source for the double-peaked light curves observed in the Type Ib SN 2008D (Bersten et al. 2013) and SN 2005bf (Folatelli et al. 2006; but see also Maeda et al. 2007).

Understanding the mixing of radioactive material is especially vital for constraining what distinguishes whether a given progenitor will explode as an SN Ib or Ic. The production of He I lines in SN spectra requires non-thermal excitation of the helium atoms, likely from the γ -rays produced by the radioactive decay of ^{56}Ni (e.g., Lucy 1991; Dessart et al. 2012; Hachinger et al. 2012). Thus, in order to produce an SN Ib, mixing may be required, while the observation of an SN Ic may not necessarily imply that its progenitor was He-poor. Early observations that constrain mixing in a normal SN Ic can therefore help to distinguish whether or not these events have an intrinsically lower helium abundance.

Thus, particularly when they are coupled with other multiwavelength observations, early light curves offer us

insight into topics such as the evolutionary path of the progenitor, the explosion mechanism, and the properties that dictate whether a given star will explode as an SN Ib or Ic. In this paper we present detailed observations of the Type Ib/c SN 2013ge, which span radio to X-ray and include spectroscopy and UV–optical photometry beginning 2–4 days after the epoch of first light. These early observations show behavior that has not been observed in any SN Ib/c to date: a distinct light curve component visible in the blue bands for the first week after explosion, which—on its rising portion—shows spectral features with moderately high expansion velocities but narrow line widths.

In Section 2 we describe the observations obtained for SN 2013ge. In Sections 3 and 4 we describe the photometric and spectroscopic properties of SN 2013ge, respectively, while in Section 5 we examine the properties of the circumstellar medium (CSM) surrounding the progenitor star. In Section 6 we discuss the consequences of various observed properties on our understanding of the progenitor of SN 2013ge.

2. OBSERVATIONS

2.1. UV and Optical Photometry

We obtained UV and optical photometric observations of SN 2013ge from a wide variety of instruments, spanning 466 days. In the sections below we describe the data acquisition, reduction, and calibration for each instrument, and in Section 2.1.6 we discuss the consistency of the combined light curve. The location of the transient on the outskirts of NGC 3287 is shown in Figure 1.

2.1.1. Discovery Photometry and Pre-explosion Limit

SN 2013ge was discovered by Koichi Itagaki on 2013 November 8.8 (all times UT) using the 0.5 m reflector at the Takanezawa station, Tochigi-ken, and was undetected prior to discovery on 2013 November 1.7 with the same instrument (CBAT 3601). We have reanalyzed these unfiltered images for this manuscript. We performed point-spread function (PSF) photometry on the SN and nearby field stars in the discovery image using standard packages in IRAF,¹⁴ and absolute calibration was performed using Bessell *R*-band magnitudes of nearby field stars. No formal color correction to the Bessell system was performed. This same procedure was also carried out on fake sources injected into the pre-discovery image. This yields an unfiltered discovery magnitude of 16.9 ± 0.1 mag and a pre-explosion limit of 19.0 mag.

2.1.2. Swift-UVOT Photometry

We observed SN 2013ge with the UV Optical Telescope (UVOT) on board *Swift* (Gehrels et al. 2004; Roming et al. 2005) from 2013 November 11 to December 9 (−11 to +17 days). The *Swift*-UVOT photometric data were extracted following the prescriptions of Brown et al. (2009). We used a variable aperture with radius 3″–5″ to maximize the signal-to-noise ratio as the SN flux faded. The *Swift*-UVOT photometry is reported in Table 1 in the photometric system described in Breeveld et al. (2011).

¹⁴ IRAF is distributed by NOAO, which is operated by the Association for Research in Astronomy, Inc., under cooperative agreement with the NSF.

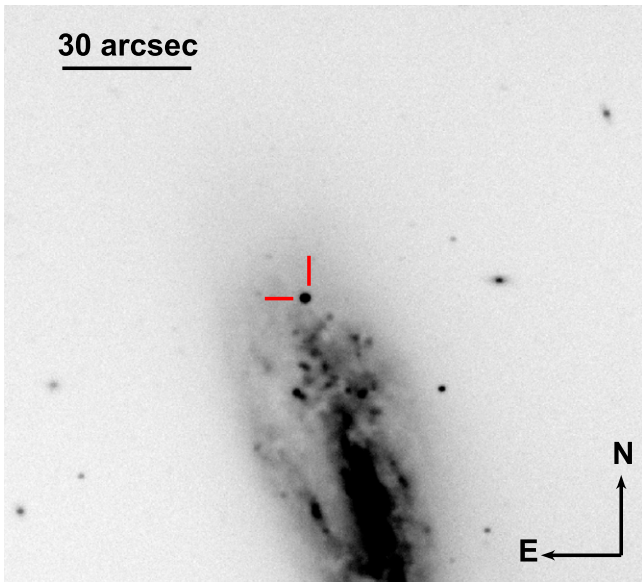


Figure 1. The r -band image from MMTCam, obtained on 2014 April 1, showing the location of SN 2013ge (red crosshairs) on the outskirts of NGC 3287.

2.1.3. Challis Observatory Optical Photometry

We observed SN 2013ge with the Challis Astronomical Observatory (CAO) on 12 nights spanning 2013 November 12 to December 14 (−10 to +22 days). CAO is located in central Idaho near the River of No Return Wilderness. The facility telescope is a 0.4 m $f/10$ Meade LX-200, equipped with an Apogee Alta U47-MB camera and $UBVRI$ Bessell filters.

For each epoch, 5–10 raw images were stacked and PSF photometry was performed in IRAF. Absolute calibration was performed using Sloan Digital Sky Survey (SDSS) observations of field stars, which were converted to the Bessell $BVRI$ system using the equations of Smith et al. (2002). A single nightly zero-point offset was applied, as data were not available to fully calibrate color terms between the CAO and standard Bessell filters. However, no strong trends between zero point and color were evident in observations of ~ 15 field stars on multiple epochs, and the observed color of SN 2013ge is well matched to the range of colors of the field stars used for calibration. We estimate that the error in our calibration (assuming a range of possible color terms) is $\lesssim 0.05$ mag over the epochs we observed with CAO. These data are listed in Table 2 in the Bessell photometric system.

2.1.4. FLWO 1.2 m Optical Photometry

We obtained 55 epochs of $BVri$ photometry of SN 2013ge spanning 2013 December 7 to 2014 May 3 (+15 to +162 days) with the Fred Lawrence Whipple Observatory (FLWO) 1.2 m telescope plus KeplerCam CCD. The KeplerCam data were reduced using IRAF, IDL, and PERL procedures as described in Hicken et al. (2012) for the CfA4 Type Ia sample, with the exception that no host galaxy subtraction was performed. $BVri$ instrumental magnitudes were measured using PSF fitting. For calibration, we applied a set of linear transforms, which account for zero-point, atmospheric, and color terms. These linear transforms were calibrated using Landolt (1992) standards for BV and Smith et al. (2002) standards for r and i bands on five photometric nights, while nightly zero points

were determined by measuring the magnitudes of local comparison stars in the SN 2013ge field (for further discussion of the calibration applied, see Hicken et al. 2012). The resulting BV data in the Bessell photometric system and ri data in the SDSS photometric system are listed in Table 3.

2.1.5. MMTCam, LBT, and IMACS Optical Photometry

In addition, we obtained eight epochs of ri -band photometry and two epochs of z -band photometry with the MMTCam instrument mounted on the 6.5 m MMT telescope, one epoch of ri -band imaging with the Large Binocular Camera (LBC; Speziali et al. 2008) mounted on the Large Binocular Telescope (LBT), and two epochs of r -band imaging with IMACS on Magellan-Baade. One epoch was obtained on 2013 November 19 (−3 days), and the other epochs span 2013 April 1 to 2015 April 16 (+129 to +510 days). Bias and flat-field corrections were made to all images, and nightly stacks were produced using standard routines in IRAF. Dark frame corrections were also applied to images taken with MMTCam. PSF photometry was performed and absolute calibration was carried out using SDSS observations of field stars. A single nightly zero-point offset was performed. These data are listed in the SDSS photometric system in Table 4.

2.1.6. Combined UV–Optical Light Curve

As a result of the extensive observations described above, we possess *Swift*-UVOT data in the Breeveld et al. (2011) photometric system, CAO $BVRI$ and FLWO BV data in the Bessell photometric system, and FLWO ri , MMTCam riz , LBT ri , and IMACS r -band data in the SDSS photometric system. We plot the resulting UV/optical light curve in Figure 2. In this figure color signifies the observed band, and the shape of the symbol signifies the source of the photometry (see legend). In order to place data from different photometric systems on the same plot, we have shifted the photometric zero point of all data to the AB magnitude scale ($m = -2.5 \log_{10} (F_{\text{Jy}}/3630)$) and have corrected for the extinction in each observed band based on the total $E(B - V) = 0.067$ mag derived in Section 2.6. We find good agreement between our data from different sources. Slight variations, on the order of 0.05–0.1 mag, are observed between the *Swift* bv data and CAO BV data, as expected for the different filter curves. We note that the overlapping epochs of CAO/FLWO V -band data and FLWO/MMTCam ri -band data agree within the quoted uncertainties, consistent with the conclusion that the color corrections between the CAO/MMTCam filters and the standard Bessell/SDSS filters are small.

The unfiltered discovery photometry and pre-explosion limit are shown as a hexagon with an asterisk and an open downward-pointing triangle in Figure 2, respectively. These points have been processed in the same manner as the R -band data for placement on this plot, but we caution that some variations likely exist between these data and the standard Bessell R band at early times when the SN is very blue. We do not attempt to transform all of our data to a single photometric/filter system. In the analysis below, each point is treated appropriately for the filter in which it was originally observed.

2.2. Chandra X-Ray Observations

We obtained deep X-ray limits for SN 2013ge with the *Chandra* X-ray Observatory on 2013 December 7 under an

Table 1
Swift-UVOT Photometry

UT Date	MJD	<i>uvw2</i> (err) (mag)	<i>uvm2</i> (err) (mag)	<i>uvw1</i> (err) (mag)	<i>u</i> (err) (mag)	<i>b</i> (err) (mag)	<i>v</i> (err) (mag)
2013 Nov 11	56,607.0	16.66 (0.08)	15.34 (0.06)
2013 Nov 11	56,607.8	17.32 (0.07)	17.37 (0.06)	16.20 (0.06)	15.03 (0.04)	15.79 (0.04)	15.69 (0.06)
2013 Nov 12	56,608.7	17.21 (0.07)	17.36 (0.07)	16.18 (0.06)	14.94 (0.04)	15.61 (0.04)	15.54 (0.06)
2013 Nov 13	56,609.8	17.29 (0.07)	17.40 (0.07)	16.11 (0.05)	14.87 (0.04)	15.56 (0.04)	15.32 (0.05)
2013 Nov 14	56,610.8	17.37 (0.08)	17.46 (0.10)	16.25 (0.06)	15.03 (0.05)	15.55 (0.04)	15.20 (0.05)
2013 Nov 15	56,611.3	17.53 (0.08)	17.50 (0.08)	16.44 (0.07)	15.05 (0.05)	15.46 (0.04)	15.26 (0.05)
2013 Nov 16	56,612.1	17.54 (0.08)	17.70 (0.08)	16.55 (0.07)	15.21 (0.05)	15.43 (0.04)	15.15 (0.05)
2013 Nov 17	56,613.1	17.57 (0.08)	17.93 (0.12)	16.69 (0.07)	15.26 (0.05)	15.46 (0.04)	15.11 (0.05)
2013 Nov 18	56,614.6	17.72 (0.08)	...	16.79 (0.07)	15.30 (0.05)	15.47 (0.04)	14.98 (0.05)
2013 Nov 19	56,615.1	17.76 (0.08)	18.07 (0.09)	16.80 (0.07)	15.39 (0.05)	15.42 (0.04)	14.94 (0.04)
2013 Nov 20	56,616.7	17.86 (0.09)	17.92 (0.09)	16.82 (0.07)	15.39 (0.05)	15.51 (0.04)	14.95 (0.05)
2013 Nov 21	56,617.1	17.75 (0.08)	17.94 (0.09)	16.85 (0.07)	15.42 (0.05)	15.36 (0.04)	14.83 (0.04)
2013 Nov 22	56,618.6	16.83 (0.06)	15.46 (0.04)	15.39 (0.04)	14.78 (0.06)
2013 Nov 23	56,619.2	16.98 (0.06)	15.47 (0.04)	15.38 (0.04)	14.87 (0.08)
2013 Nov 24	56,620.1	17.15 (0.07)	15.61 (0.04)	15.54 (0.04)	14.76 (0.07)
2013 Nov 27	56,623.1	17.25 (0.08)	15.84 (0.05)	15.55 (0.04)	14.81 (0.04)
2013 Nov 29	56,625.9	17.40 (0.08)	16.16 (0.05)	15.77 (0.05)	14.93 (0.06)
2013 Dec 1	56,627.7	17.39 (0.07)	16.49 (0.05)	16.07 (0.04)	15.00 (0.05)
2013 Dec 3	56,629.5	17.38 (0.07)	16.70 (0.05)	16.10 (0.04)	15.03 (0.06)
2013 Dec 5	56,631.1	17.61 (0.08)	16.77 (0.06)	16.30 (0.05)	15.24 (0.06)
2013 Dec 7	56,633.5	17.74 (0.10)	16.91 (0.07)	16.46 (0.06)	15.36 (0.06)
2013 Dec 9	56,635.2	17.90 (0.10)	17.08 (0.07)	16.62 (0.06)	15.48 (0.07)

Note. Data are presented in the photometric system of Breeveld et al. (2011).

approved Director Discretionary Time Proposal (PI: Margutti). The total exposure time was 18.8 ks. *Chandra* ACIS-S data were reduced with the CIAO software package (v4.5) and relevant calibration files, applying standard filtering criteria. Using *wavdetect*, we find no evidence for X-ray emission at the location of SN 2013ge. The 3σ count-rate upper limit is $3.1 \times 10^{-4} \text{ s}^{-1}$ in the 0.5–8 keV energy band.

The neutral hydrogen column density in the direction of the SN is $\text{NH}_{\text{gal}} = 1.9 \times 10^{20} \text{ cm}^{-2}$ (Kalberla et al. 2005). From our optical spectra we estimate $E(B - V)_{\text{host}} = 0.047 \text{ mag}$ (Section 2.6). For a Galactic dust-to-gas ratio, this value corresponds to an intrinsic neutral hydrogen column density of $\text{NH}_{\text{host}} \sim 3 \times 10^{20} \text{ cm}^{-2}$. For an assumed simple power-law spectral model with spectral photon index $\Gamma = 2$ we find an unabsorbed flux limit of $3.4 \times 10^{-15} \text{ erg s}^{-1} \text{ cm}^{-2}$ (0.3–10 keV). At the distance of 23.7 Mpc (Section 2.6), this flux translates into a luminosity limit of $2.3 \times 10^{38} \text{ erg s}^{-1}$.

2.3. Very Large Array Radio Observations

We obtained three epochs of deep radio limits for the emission from SN 2013ge at 4.8 and 7.1 GHz with the Very Large Array (VLA).¹⁵ Observations were obtained on 2013 November 16 and 25 and 2014 January 14 (−6, +3, and +53 days), when the VLA was in B configuration, under program 13A-270.

All observations were taken in standard continuum observing mode with a bandwidth of $16 \times 64 \times 2 \text{ MHz}$. During the reduction, we split the data into two basebands of approximately 1 GHz each.¹⁶ We used 3C 286 for flux calibration and calibrator J1018+3542 for phase referencing. The data were

reduced using standard packages within the Astronomical Image Processing System (AIPS). No radio emission was detected from SN 2013ge in any of these observations. We measured the rms noise at the location of SN 2013ge in each image using the task “JMFIT” in AIPS. The resulting 3σ upper limits for each frequency and epoch are listed in Table 5.

2.4. Optical Spectroscopy

We obtained 29 epochs of low-resolution optical spectra for SN 2013ge, spanning −13 to +447 days. In addition, one moderate-resolution ($R \sim 3400$) spectrum was obtained at −12 days in the region of Na ID. All optical spectra are listed in Table 6 and are shown in Figure 3. All long-slit observations were carried out with the slit oriented at the parallactic angle, with the exception of those obtained on *Magellan*/IMACS, which possesses an atmospheric dispersion corrector.

Initial reduction (overscan correction, flat-fielding, extraction, wavelength calibration) for all long-slit spectra was carried out using the standard packages in IRAF. The MODS/LBT spectrum was taken in the dual-channel mode with gratings G400L and G670L, and we used the modsCCDRed suite of python programs to perform bias subtraction and flat-field correction and adjust for bad columns, before extracting the spectrum using standard packages in IRAF. Flux calibration and telluric correction for all long-slit spectra were performed using a set of custom IDL scripts (see, e.g., Matheson et al. 2008; Blondin et al. 2012) and standard star observations obtained the same night as the science exposures. Spectra obtained with the Hectospec multifiber spectrograph (Fabricant et al. 2005) were reduced using the IRAF package “hectospec” and the CfA pipeline designed for this instrument. In all cases, when possible, spectroscopic flux calibration has been checked against observed photometry.

¹⁵ The National Radio Astronomy Observatory is a facility of the National Science Foundation operated under cooperative agreement by Associated Universities, Inc.

¹⁶ $8 \text{ IF} \times 64 \text{ (channels/IF)} \times 2 \text{ (MHz/channel)}$.

Table 2
CAO Photometry

UT Date	MJD	<i>B</i> (err) (mag)	<i>V</i> (err) (mag)	<i>R</i> (err) (mag)	<i>I</i> (err) (mag)
2013 Nov 12	56,608.5	...	15.62 (0.09)	15.67 (0.13)	15.43 (0.22)
2013 Nov 22	56,618.5	15.51 (0.10)	14.88 (0.08)	14.70 (0.05)	14.41 (0.05)
2013 Nov 23	56,619.5	15.46 (0.09)	14.80 (0.07)	14.55 (0.04)	14.33 (0.06)
2013 Nov 24	56,620.5	15.53 (0.09)	14.83 (0.07)	14.51 (0.06)	14.30 (0.05)
2013 Nov 25	56,621.5	15.64 (0.14)	14.87 (0.06)	14.68 (0.06)	14.35 (0.08)
2013 Nov 26	56,622.5	15.63 (0.09)	14.82 (0.10)	14.66 (0.05)	14.33 (0.05)
2013 Nov 28	56,624.5	15.83 (0.10)	14.94 (0.06)	14.58 (0.04)	14.25 (0.05)
2013 Nov 29	56,625.5	15.93 (0.12)	14.96 (0.10)	14.58 (0.05)	14.27 (0.06)
2013 Dec 5	56,631.5	...	15.41 (0.14)	14.80 (0.10)	14.42 (0.16)
2013 Dec 11	56,637.5	...	15.60 (0.21)	14.98 (0.15)	14.56 (0.19)
2013 Dec 12	56,638.5	...	15.85 (0.09)	15.09 (0.06)	14.63 (0.09)
2013 Dec 14	56,640.5	...	15.87 (0.09)	15.10 (0.06)	14.64 (0.09)

Note. Data are presented in the Bessell photometric system.

2.5. Infrared Spectroscopy

We obtained eight epochs of near-IR (NIR) spectra for SN 2013ge with the Folded-port InfraRed Echellette spectrograph (FIRE; Simcoe et al. 2013) on *Magellan-Baade* spanning -2 to $+123$ days. All observations were obtained in long-slit mode with the slit orientated at the paratactic angle. These data were reduced following standard procedures (see, e.g., Hsiao et al. 2015) using an IDL pipeline designed specifically for FIRE (firehose).¹⁷ A0V standards observed with each science exposure were used to correct for telluric absorption using the IDL tool `xtellcor` (Vacca et al. 2003). A model spectrum of Vega was used to remove stellar absorption features from the telluric standards, and the resulting spectra were also used for flux calibration. All NIR spectra are listed in Table 6 and shown in Figure 4.

2.6. Distance and Reddening

SN 2013ge exploded on the outskirts of NGC 3287. In this paper we adopt a distance of 23.7 ± 1.7 Mpc, corresponding to the NED distance after correction for Virgo, Great Attractor, and Shapley Supercluster infall, assuming $H_0 = 73 \text{ km s}^{-1} \text{ Mpc}^{-1}$ (Mould et al. 2000).

Milky Way reddening in the direction of SN 2013ge is $E(B - V)_{\text{MW}} = 0.020$ mag (Schlafly & Finkbeiner 2011). To estimate the intrinsic absorption due to dust within NGC 3287, we examine our moderate-resolution spectra obtained on 2014 November 10 for narrow Na ID absorption lines. We identify two Na ID $\lambda\lambda 5889.9, 5895.9$ doublets, one corresponding to Milky Way absorption, and one at the redshift of NGC 3287. The total equivalent width of the Na ID doublet at the redshift of NGC 3287 is $\sim 0.45 \text{ \AA}$. Using the empirical relation of Poznanski et al. (2012), this implies a host galaxy contribution to the total reddening of $E(B - V)_{\text{host}} = 0.047$ mag. As a check, we apply the same procedure to the observed Milky Way Na ID absorption, which yields an $E(B - V)_{\text{MW}}$ value of 0.037 mag. This value is slightly higher than that found by Schlafly & Finkbeiner (2011), but within the quoted errors of the relation from Poznanski et al. (2012). Throughout this paper we adopt an $R = A_V/E(B - V) = 3.1$ Milky Way extinction curve with a total reddening of $E(B - V)_{\text{tot}}$

$= 0.067$ mag. This value is consistent with that derived from the $V - R$ color method described in Drout et al. (2011).

3. PHOTOMETRIC PROPERTIES

3.1. light curve Evolution

A deep pre-explosion limit for SN 2013ge was obtained 7 days prior to its initial discovery. However, the rapid rise observed in the *Swift* *u* and *w1* bands (photometric coverage in these bands began ~ 2 days after first detection; see Figure 5) indicates that our constraints on the epoch of first light may be more stringent than allowed by this nondetection alone. Extrapolating polynomial fits of the rising phase of these light curves backward in time, we infer an epoch of first light only ~ 2 days prior to first detection. Power-law fits of the form $L_\lambda \propto t^{1.5}$ and $L_\lambda \propto t^2$ yield similar results. The former power law is expected for the rising phase of cooling envelope emission (e.g., Piro & Nakar 2013), and the latter is expected for early radioactive heating in the fireball model (Nugent et al. 2011). Throughout this paper we adopt an epoch of first light of 2014 November 6.5 = MJD 56,602.5 ± 2 days. An epoch of first light prior to this date would be inconsistent with the early *u*- and *w1*-band light curves unless the rate of rise *increased* sometime post-explosion. Such behavior is not typically observed in SN light curves and would have implications for the early emission source, which will be discussed in Section 6. The possibility of a “dark period” separating the epoch of first light from the explosion epoch (Piro & Nakar 2013) will be also discussed in Section 6.

In Table 7 we list basic properties for the UV and optical light curves of SN 2013ge, which were measured based on low-order polynomial fits.¹⁸ Throughout this paper, the phase of the SN will be given with respect to *V*-band maximum light: MJD 56,618.6. This time of maximum implies a rise time in the *V* band of ~ 16 days. As is observed in other SNe I, the time of maximum light cascades through the UV and optical bands (as shown by the dot-dashed line in Figure 2). SN 2013ge peaks at an absolute magnitude of approximately -17.3 mag (AB) in the optical and declines between 1.1 and 0.38 mag in the first 15 days post-

¹⁷ Available at <http://web.mit.edu/~rsimcoe/www/FIRE/>.

¹⁸ Polynomial fits for each band were performed based on photometry for a single source, as listed in Table 7.

Table 3
FLWO Photometry

UT Date	MJD	<i>B</i> (err) (mag)	<i>V</i> (err) (mag)	<i>r'</i> (err) (mag)	<i>i'</i> (err) (mag)
2013 Dec 7	56,633.4	16.70 (0.02)	15.54 (0.02)	15.15 (0.03)	15.06 (0.03)
2013 Dec 7	56,633.5	16.71 (0.03)	15.55 (0.03)	15.15 (0.05)	15.08 (0.04)
2013 Dec 8	56,634.4	16.70 (0.02)	15.54 (0.02)	15.14 (0.01)	15.04 (0.01)
2013 Dec 14	56,640.3	17.16 (0.02)	15.93 (0.02)	15.47 (0.02)	15.35 (0.03)
2013 Dec 23	56,649.5	17.36 (0.03)	16.27 (0.01)	15.85 (0.01)	15.72 (0.01)
2013 Dec 24	56,650.5	17.57 (0.03)	16.35 (0.02)	15.91 (0.03)	15.78 (0.03)
2013 Dec 26	56,652.5	17.54 (0.02)	16.36 (0.01)	15.93 (0.01)	15.84 (0.02)
2013 Dec 27	56,653.5	17.53 (0.02)	16.40 (0.01)	15.95 (0.01)	15.85 (0.01)
2013 Dec 28	56,654.5	17.62 (0.02)	...	16.02 (0.03)	15.91 (0.03)
2013 Dec 29	56,655.5	15.92 (0.05)
2013 Dec 30	56,656.3	17.52 (0.02)	16.42 (0.01)	15.96 (0.01)	15.84 (0.01)
2014 Jan 1	56,658.5	17.65 (0.02)	16.48 (0.02)	16.08 (0.02)	...
2014 Jan 2	56,659.5	...	16.49 (0.01)	16.07 (0.01)	15.99 (0.01)
2014 Jan 3	56,660.3	17.71 (0.04)	16.54 (0.03)	16.13 (0.04)	15.93 (0.02)
2014 Jan 6	56,663.5	17.71 (0.02)	16.58 (0.05)	16.19 (0.05)	16.10 (0.06)
2014 Jan 9	56,666.4	17.76 (0.03)	16.64 (0.02)	...	16.19 (0.03)
2014 Jan 11	56,668.3	17.76 (0.02)	16.65 (0.01)	16.29 (0.02)	16.23 (0.02)
2014 Jan 12	56,669.5	17.80 (0.03)	16.70 (0.03)	16.30 (0.03)	16.27 (0.04)
2014 Jan 13	56,670.5	17.78 (0.02)	16.70 (0.03)	16.34 (0.02)	16.31 (0.03)
2014 Jan 14	56,671.4	17.83 (0.03)	16.73 (0.04)	16.38 (0.04)	16.32 (0.04)
2014 Jan 15	56,672.5	...	16.70 (0.01)	16.32 (0.01)	16.29 (0.01)
2014 Jan 16	56,673.5	17.88 (0.04)	16.78 (0.03)	16.44 (0.05)	...
2014 Jan 17	56,674.4	...	16.69 (0.01)	16.27 (0.02)	16.35 (0.01)
2014 Jan 18	56,675.4	17.85 (0.03)	16.77 (0.02)	16.44 (0.03)	16.44 (0.03)
2014 Jan 19	56,676.5	...	16.82 (0.03)	...	16.50 (0.04)
2014 Jan 20	56,677.4	17.92 (0.04)	16.85 (0.03)	16.49 (0.03)	16.48 (0.03)
2014 Jan 21	56,678.4	17.89 (0.02)	...	16.50 (0.02)	16.49 (0.02)
2014 Jan 23	56,680.4	17.86 (0.02)	16.87 (0.02)	16.53 (0.03)	16.55 (0.03)
2014 Jan 26	56,683.5	17.92 (0.02)	16.91 (0.03)	16.59 (0.03)	16.61 (0.02)
2014 Jan 28	56,685.4	17.90 (0.02)	16.95 (0.02)	16.60 (0.03)	16.63 (0.03)
2014 Feb 3	56,691.3	17.97 (0.02)	17.00 (0.02)	16.70 (0.02)	16.77 (0.03)
2014 Feb 6	56,694.4	...	17.05 (0.03)
2014 Feb 9	56,697.4	18.08 (0.02)	17.13 (0.02)	16.81 (0.02)	16.89 (0.02)
2014 Feb 12	56,700.3	18.14 (0.02)	17.20 (0.02)	16.87 (0.02)	16.96 (0.02)
2014 Feb 13	56,701.4	18.16 (0.03)	17.21 (0.03)	16.89 (0.03)	17.01 (0.04)
2014 Feb 14	56,702.3	18.20 (0.03)	17.21 (0.03)	16.90 (0.02)	17.03 (0.03)
2014 Feb 15	56,703.5	18.18 (0.04)
2014 Feb 18	56,706.4	18.20 (0.02)	17.28 (0.03)	16.97 (0.03)	17.09 (0.04)
2014 Feb 20	56,708.5	18.11 (0.02)	17.31 (0.02)	17.02 (0.02)	17.15 (0.03)
2014 Feb 25	56,713.2	18.19 (0.03)	17.34 (0.04)	17.05 (0.03)	17.15 (0.02)
2014 Feb 25	56,713.3	18.30 (0.03)	17.42 (0.05)	17.07 (0.03)	...
2014 Feb 27	56,715.2	18.24 (0.03)	17.35 (0.02)	17.07 (0.02)	17.22 (0.02)
2014 Feb 27	56,715.5	18.28 (0.03)	17.39 (0.02)	17.11 (0.02)	17.25 (0.03)
2014 Mar 5	56,721.5	17.08 (0.02)	17.24 (0.02)
2014 Mar 6	56,722.3	18.38 (0.03)	17.54 (0.04)	17.19 (0.04)	17.35 (0.03)
2014 Mar 14	56,730.5	18.50 (0.04)	17.67 (0.03)	17.29 (0.02)	17.60 (0.04)
2014 Mar 15	56,731.4	...	17.63 (0.03)
2014 Mar 17	56,733.3	18.63 (0.04)	17.77 (0.03)	17.38 (0.03)	17.62 (0.03)
2014 Mar 19	56,735.3	18.50 (0.05)	17.77 (0.07)	17.33 (0.07)	17.61 (0.13)
2014 Mar 25	56,741.3	18.68 (0.03)	17.88 (0.04)	17.50 (0.04)	17.71 (0.03)
2014 Mar 30	56,746.3	18.73 (0.10)	17.75 (0.05)
2014 Apr 2	56,749.3	18.64 (0.03)	18.00 (0.02)	17.58 (0.02)	17.71 (0.02)
2014 Apr 7	56,754.3	18.64 (0.03)	18.00 (0.02)	17.57 (0.02)	17.91 (0.03)
2014 Apr 30	56,777.2
2014 May 3	56,780.2	19.46 (0.03)	18.70 (0.02)	18.12 (0.03)	18.39 (0.03)

Note. *BV* data are presented in the Bessell photometric system, and *ri* data are presented in the SDSS photometric system.

maximum light (*b* through *I* bands, respectively). This places SN 2013ge at both the low-luminosity and slowly evolving end of SNe I.

The *BVRI* light curves are characterized by a smooth rise to maximum light, followed by an initial decline and then a

shallowing of the slope between 20 and 30 days post-maximum light. Linear fits to the *BVRI* light curves between 60 and 120 days post-maximum reveal linear decline rates between 0.01 and 0.02 mag day⁻¹. This light curve morphology is typical for SNe I.

Table 4
MMTCam, LBT, and IMACS Photometry

UT Date	MJD	r (err) (mag)	i (err) (mag)	z (err) (mag)	Instrument
2013 Nov 19	56,615.5	15.01 (0.03)	14.98 (0.04)	15.04 (0.05)	MMTCam
2014 Apr 1	56,748.1	17.59 (0.05)	17.85 (0.02)	...	MMTCam
2014 Apr 4	56,751.3	17.69 (0.03)	17.91 (0.02)	17.04 (0.01)	MMTCam
2014 May 21	56,798.2	18.41 (0.02)	18.71 (0.03)	...	MMTCam
2014 Jun 7	56,815.1	18.71 (0.04)	18.92 (0.01)	...	MMTCam
2014 Oct 22	56,952.1	20.48 (0.05)	20.96 (0.02)	...	LBT
2014 Nov 20	56,981.5	21.18 (0.03)	21.62 (0.03)	...	MMTCam
2014 Dec 18	57,009.3	21.36 (0.02)	IMACS
2015 Jan 15	57,037.3	21.65 (0.03)	IMACS
2015 Feb 10	57,063.4	22.13 (0.06)	22.58 (0.04)	...	MMTCam
2015 Apr 16	57,128.1	>22.3	>22.4	...	MMTCam

Note. Data are presented in the SDSS photometric system.

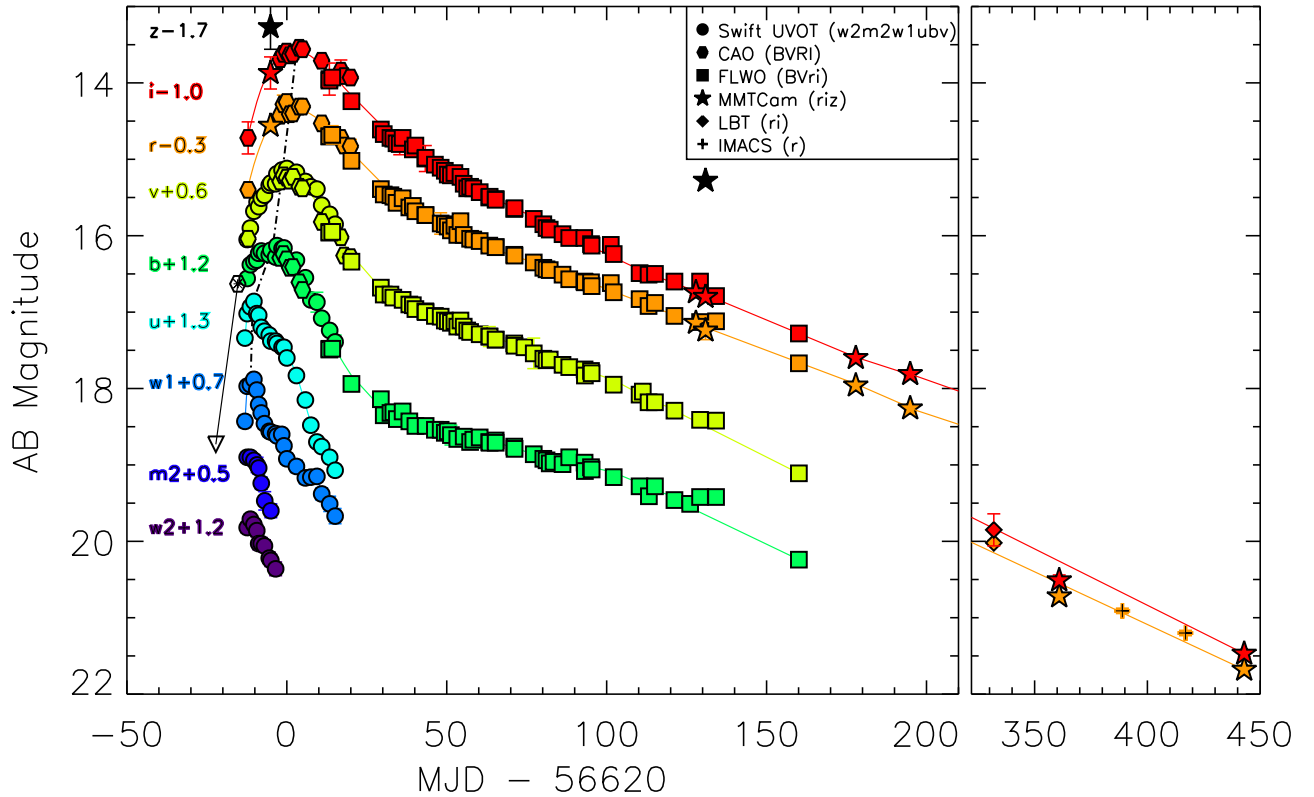


Figure 2. Multiband photometry for SN 2013ge. Symbol shape indicates the source of the photometry, and color indicates the observed band, as labeled. The unfiltered discovery photometry and pre-explosion limit are shown as a hexagon with an asterisk and an open downward-pointing triangle, respectively. See Section 2.1.6 for further information on the procedures applied to place data on this plot. The dot-dashed line traces the epoch of maximum light for each observed band.

Table 5
VLA Observations

UT Date	MJD	Frequency GHz	F_ν^a μJy
2013 Nov 16	56,612.8	4.8	<45.6
...	...	7.1	<42.0
2013 Nov 26	56,622.4	4.8	<36.0
...	...	7.1	<30.9
2014 Jan 4	56,661.3	4.8	<36.0
...	...	7.1	<29.3

Note.

^a All quoted flux limits are 3σ .

3.2. Early UV Light Curves

In contrast, the u - and $w1$ -band light curves observed for SN 2013ge show a distinctly nonstandard evolution. They display an early “bump” that is characterized by a rapid rise and decline over the first week of observations, before plateauing and then falling off rapidly again. In the top panel of Figure 6 we demonstrate that the u -band light curve can be decomposed into two components: a main component that peaks ~ 11 days after discovery superimposed with an early peak of emission that rises rapidly over ~ 4 days and declines rapidly after ~ 1 week. This particular decomposition is for illustrative purposes only, as we do not constrain the

Table 6
Optical and Infrared Spectroscopy

UT Date	MJD	Telescope	Instrument ^a
2013 Nov 9	56,605	MMT	BC
2013 Nov 10	56,606	MMT	BC ^b
2013 Nov 10	56,606	MMT	BC
2013 Nov 11	56,607	MMT	BC
2013 Nov 20	56,616	Magellan-Baade	FIRE
2013 Nov 21	56,617	MMT	Hectospec
2013 Nov 29	56,625	MMT	Hectospec
2013 Nov 30	56,626	Magellan-Baade	FIRE
2013 Dec 6	56,632	Tillinghast 60-inch	FAST
2013 Dec 7	56,633	Tillinghast 60-inch	FAST
2013 Dec 9	56,634	Magellan-Baade	FIRE
2013 Dec 10	56,636	Tillinghast 60-inch	FAST
2013 Dec 13	56,639	MDM 2.4 m	OSMOS
2013 Dec 24	56,650	MMT	BC
2013 Dec 27	56,653	MMT	BC
2013 Dec 28	56,654	MMT	BC
2013 Dec 31	56,657	Magellan-Clay	LDSS-3
2014 Jan 1	56,658	Magellan-Baade	FIRE
2014 Jan 3	56,660	Tillinghast 60-inch	FAST
2014 Jan 6	56,663	Tillinghast 60-inch	FAST
2014 Jan 7	56,664	Tillinghast 60-inch	FAST
2014 Jan 9	56,666	Tillinghast 60-inch	FAST
2014 Jan 9	56,666	Magellan-Baade	FIRE
2014 Jan 25	56,682	Shane 3 m	Kast
2014 Jan 28	56,685	Tillinghast 60-inch	FAST
2014 Jan 30	56,687	Tillinghast 60-inch	FAST
2014 Feb 2	56,690	Tillinghast 60-inch	FAST
2014 Feb 2	56,690	Magellan-Baade	FIRE
2014 Feb 3	56,691	Magellan-Baade	IMACS
2014 Feb 26	56,714	Tillinghast 60-inch	FAST
2014 Feb 27	56,715	Magellan-Baade	FIRE
2014 Mar 4	56,720	Tillinghast 60-inch	FAST
2014 Mar 6	56,722	MMT	BC
2014 Mar 7	56,723	Tillinghast 60-inch	FAST
2014 Mar 25	56,741	Magellan-Baade	FIRE
2014 Apr 28	56,775	MMT	BC
2014 Oct 23	56,953	LBT	MODS
2015 Jan 15	57,037	Magellan-Baade	IMACS

Notes.

^a Instrument references: FAST spectrograph (Fabricant et al. 1998) on the FLWO 60-inch Tillinghast telescope; Blue Channel (BC) spectrograph (Schmidt et al. 1989) on the 6.5 MMT; Hectospec multifiber spectrograph (Fabricant et al. 2005) on the MMT; Low Dispersion Survey Spectrograph-3 (LDSS-3; Allington-Smith et al. 1994) on *Magellan*-Clay, the Inamori-*Magellan* Areal Camera and Spectrograph (IMACS; Dressler et al. 2006) on *Magellan*-Baade; OSMOS on the MDM 2.4 m (Martini et al. 2011); the Kast spectrograph (Miller & Stone 1993) on Shane 3 m at Lick Observatory; Multi-Object Double Spectrograph (MODS; Pogge et al. 2010) mounted on the 2×8.4 m LBT; Folded-port InfraRed Echellette spectrograph (FIRE; Simcoe et al. 2013) on *Magellan*-Baade.

^b Observation with the 1200 line mm^{-1} grating.

rising behavior of the second component. Vertical dashed lines mark our first three epochs of spectroscopy, which probe the early rising portion of the first component.

Although well sampled *u*-band light curves between -14 and -7 days are still quite rare for SNe I, no previous object has shown two distinct components with these timescales. This is demonstrated in the bottom panel of Figure 6, where we compile *u*-band light curves from the literature. A majority of the events peak ~ 4 days prior to *V*-band maximum and then

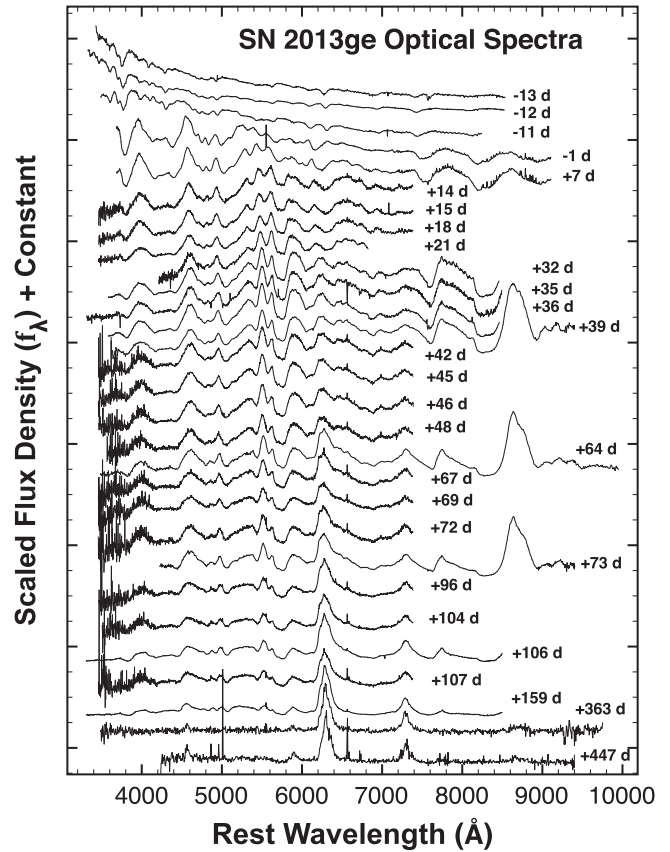


Figure 3. Normalized optical spectra spanning -13 to $+447$ days with respect to *V*-band maximum.

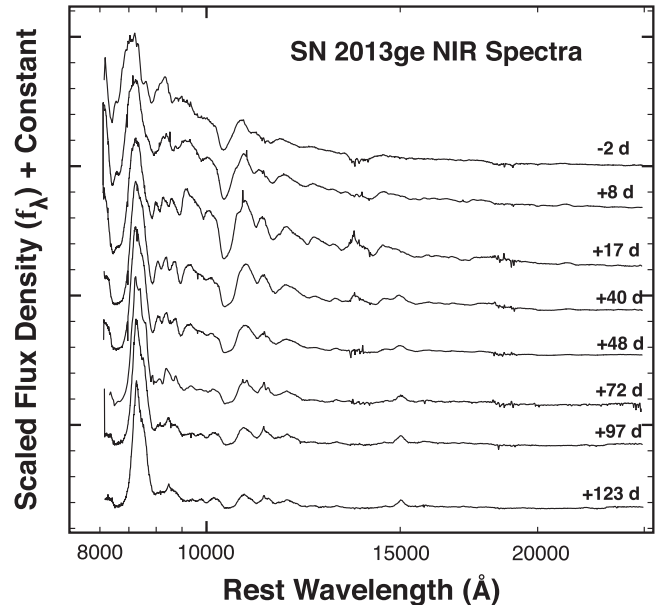


Figure 4. Normalized NIR spectra spanning -2 to $+123$ days with respect to *V*-band maximum.

decline rapidly, consistent with our inferred time of maximum and subsequent evolution for the *second* component in SN 2013ge.

Prior to this maximum, the evolution of the literature events is varied. Both SN 2008D and SN 2005bf also show double-peaked *u*-band light curves, but with timescales significantly

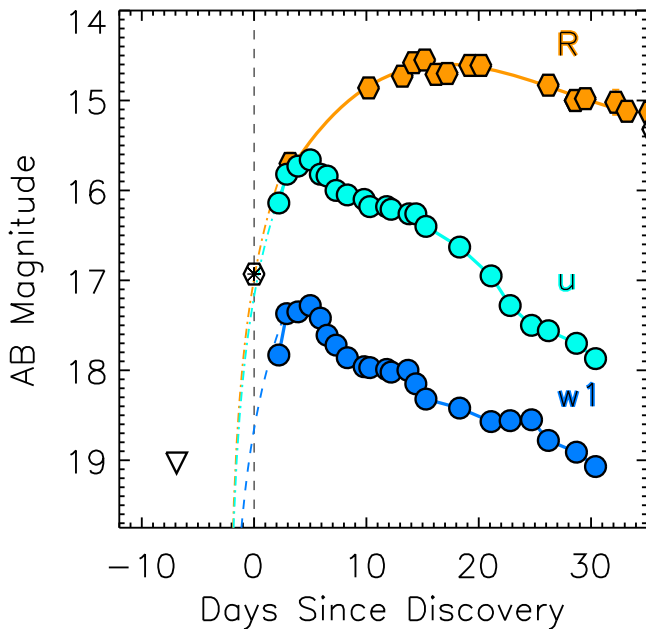


Figure 5. Characterization of the epoch of first light. Shown are the *R*-band (orange), *u*-band (cyan), and *w1*-band (blue) light curves, shifted to the AB system in the same manner as for Figure 2 (see Section 2.1.6). The rapid rise observed in the *u*- and *w1*-band light curves puts a tight constraint on the epoch of first light. Dashed colored lines are power-law fits of the form $t^{1.5}$ to the rising phase of each band, all of which imply an epoch of first light 2 days prior to first detection. The unfiltered discovery and pre-explosion limit are shown as a hexagon with an asterisk and an open triangle, respectively.

different from those observed in SN 2013ge. The first peak in the light curve of SN 2008D rises on a timescale of ~ 1 day from the observed X-ray flash, while the first light curve component of the peculiar Type Ib SN 2005bf has a rise time $\gtrsim 13$ days. The early emission from SN 2008D has been interpreted as both adiabatic cooling emission and emission associated with a double-peaked ^{56}Ni distribution. In contrast, in the model of Maeda et al. (2007), the first peak of SN 2005bf is powered by the radioactive decay of ^{56}Ni , while the second peak requires an additional power source such as a central engine. Intriguingly, the *U*-band light curve of the Type Ib SN 2009jf shows a plateau that could be consistent with two components similar to those in SN 2013ge if the luminosities were comparable.

Finally, we note that the *w1*-band light curve of SN 2013ge shows tentative evidence for multiple changes in slope over ~ 30 days. However, additional observations would be necessary to discern whether the behavior between $+20$ and $+30$ days is due to a change in input power source or variations in spectral features/line blanketing.

3.3. Color Evolution and SEDs

In Figure 7 we plot the $U - B$ and $B - V$ colors of SN 2013ge and several other SNe Ib/c. The gray shaded region highlights the time of the *u*-band excess described above. During these epochs, the $u - b$ color of SN 2013ge is relatively flat for 3 days before rapidly reddening from ~ 0.4 to ~ 0.9 mag over 4 days. The $B - V$ color evolution of SN 2013ge is similar to that of other SNe Ib/c.

In Figure 8 we plot the spectral energy distribution (SED) of SN 2013ge for epochs on the rising phase of the initial *u*-band peak (including our first three epochs of spectroscopy). The

first spectroscopic observations are characterized by a very blue continuum, while from day -11 onward the *Swift*-UVOT photometry shows that the SED falls off significantly in the UV bands. As shown in the bottom panel of Figure 8, it is not possible to fit both the slope of the optical SED and the low flux level in the UV bands with a single blackbody. Such behavior may indicate that line blanketing is significantly depressing the UV flux, even at these very early epochs.

Fitting blackbodies to the *BVRI* bands only, we find color temperatures that fall from around 13,000 K at -12 days to around 7000 K at *V*-band maximum. The precise temperature evolution during the initial *u*-band peak is difficult to assess owing to (1) the depressed UV flux and (2) our lack of dense *R*- and *I*-band photometry at the earliest epochs.

3.4. Pseudo-bolometric Light Curve

To create a pseudo-bolometric light curve, we first sum our UV-optical photometry by means of a trapezoidal integration. To account for missing IR flux, we attach a blackbody tail from the best-fit blackbody to the *BVRI* data. This method of accounting for IR flux is equivalent to adding an IR contribution that monotonically increases from 15% at early times to $\sim 50\%$ at late times. This is in line with what is found for SNe I with well-observed IR light curves (see, e.g., Valenti et al. 2008; Lyman et al. 2014). To account for UV contributions at later epochs (beyond our *Swift*-UVOT coverage), we extrapolate the observed *w2*-, *m2*-, *w1*-, and *u*-band light curves until they account for less than 0.5% of the pseudo-bolometric luminosity, at which point they are dropped from the integration. We note that the flux contained in the *w2*/*m2* bands and *w1*/*u* bands accounts for $\lesssim 1\%$ and only a few percent of the bolometric luminosity at the epoch of their final observed data points, respectively. Thus, ambiguity in the morphology of the late-time UV light curve should not significantly impact the derived light curve.

The resulting pseudo-bolometric light curve is shown in Figure 9, along with the pseudo-bolometric light curves of other SNe. Although two distinct peaks are not evident, an excess “shoulder” of emission can be seen at early times corresponding to the first *u*-band component described above. The bolometric light curve peaks at $(2.1 \pm 0.1) \times 10^{42} \text{ erg s}^{-1}$ and the total radiated energy between -12 and $+120$ days is $(8.1 \pm 0.3) \times 10^{48} \text{ erg}$.

Assuming that SN 2013ge is powered mainly by the radioactive decay of ^{56}Ni , we use the analytic models of Arnett (1982) and Valenti et al. (2008), with the corrections of Wheeler et al. (2015), to extract estimates of the explosion parameters from this pseudo-bolometric light curve. We assume that from -8 to $+20$ days SN 2013ge is in the optically thick photospheric phase (we neglect the earliest data, during the “UV bump,” when performing our fit) and utilize a constant opacity of $0.07 \text{ cm}^2 \text{ g}^{-1}$ (corresponding to the case of electron scattering). Under these assumptions, we find best-fit explosion parameters of $M_{\text{Ni}} \approx 0.12 M_{\odot}$, $M_{\text{ej}} = 2\text{--}3 M_{\odot}$, and $E_{\text{K}} = (1\text{--}2) \times 10^{51} \text{ erg}$. We have assumed a photospheric velocity at maximum of $10,000\text{--}11,000 \text{ km s}^{-1}$ in order to break the degeneracy between M_{ej} and E_{K} (see Section 4).

Inserting these best-fit parameters from the photospheric phase in the nebular model from Valenti et al. (2008), we find a predicted luminosity that is relatively consistent with our late-time (>60 days post-maximum) pseudo-bolometric light curve, although the predicted model declines more rapidly than the

Table 7
Basic Photometric Properties

Band	T_{\max} (MJD)	$m_{\text{obs,max}}$ (AB mag)	$M_{\text{abs,max}}$ (AB mag)	Δm_{15} (mag)	Neb. Decline Rate ^a (mag day ⁻¹)
w2	56,608.7 (1.1)	18.51 (0.06)	-13.36 (0.05)	>0.65	...
m2	56,607.7 (1.0)	18.40 (0.05)	-13.47 (0.05)	>0.70	...
w1	56,608.8 (1.0)	17.18 (0.04)	-14.69 (0.04)	1.23 (0.08)	...
u	56,609.4 (1.1)	15.56 (0.04)	-16.31 (0.04)	1.16 (0.05)	...
b	56,615.7 (1.5)	14.93 (0.03)	-16.94 (0.03)	1.11 (0.05)	0.0119 (0.0004)
v	56,618.6 (1.5)	14.52 (0.05)	-17.35 (0.05)	0.74 (0.11)	0.0156 (0.0003)
R	56,621.1 (1.5)	14.55 (0.03)	-17.32 (0.03)	0.44 (0.05)	0.0155 (0.0003)
I	56,623.1 (1.5)	14.54 (0.03)	-17.33 (0.03)	0.38 (0.06)	0.0198 (0.0004)

Note. Values for peak magnitudes, time of maximum, and Δm_{15} were measured from low-order polynomials to photometry from a single source for each band. For w2 through v bands, the polynomial was fit to the data from *Swift*-UVOT, while for R band and I band the polynomial was fit to CAO data. The peak magnitudes presented here have been shifted to the AB photometric zero point as described in Section 2.1.6.

^a Measured from a linear fit to the FLWO data between +60 and +120 days.

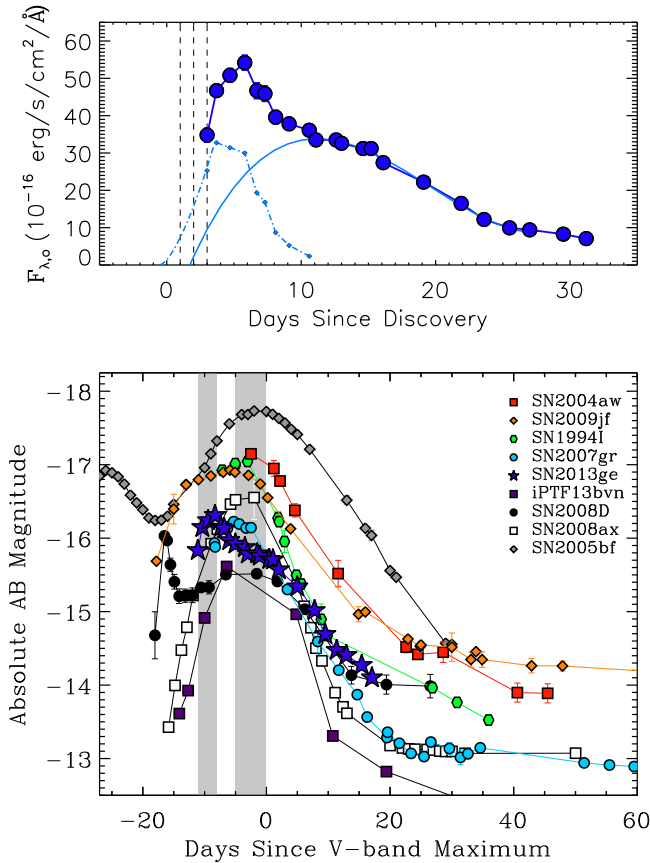


Figure 6. Top: example decomposition of the *u*-band light curve into two components. This should be taken as representative only as we do not constrain the rising behavior of the second component. Dashed vertical lines represent our first three epochs of spectroscopy, which occur on the early rising portion of the first light curve component. Bottom: comparison of the *u*-band light curve of SN 2013ge to other stripped core-collapse SNe. Shaded regions highlight the time of maximum for both components of SN 2013ge. Most events peak on a timescale similar to that observed for the second component in SN 2013ge. The light curve of SN 2009jf shows a plateau that may be indicative of an early component similar to that observed in SN 2013ge. References: SN 2005bf (Folatelli et al. 2006), SN 2004aw (Taubenberger et al. 2006), SN 2009jf (Valenti et al. 2011), SN 2007gr (Hunter et al. 2009), SN 2008ax (Pastorello et al. 2008), SN 2008D (Soderberg et al. 2008), iPTF 13bvn (Cao et al. 2013; Fremling et al. 2014). Photometry for all objects was converted to the AB system zero point before plotting.

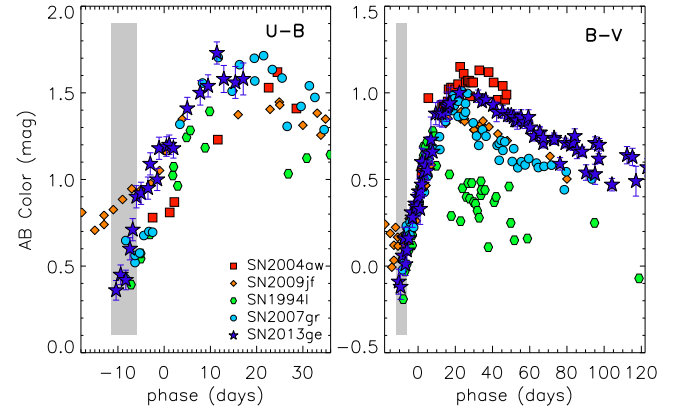


Figure 7. *u* - band *B* - *V* color evolution of SN 2013ge in comparison to other SNe Ib/c. Shaded regions indicate the time of the first light curve component. During the declining portion of the first light curve component (-8 to -5 days), the *u* - *b* color reddens drastically. The *B* - *V* evolution of SN 2013ge is very similar to other SNe Ib/c. Photometry for all objects was converted to the AB system zero point before plotting. SN 2013ge data contain *u* - *b* and *b* - *v* observations from *Swift*-UVOT, as well as Bessell *B* - *V* data from CAO and FLWO. All literature objects were observed with Bessell filters (see Figure 6 for references).

observed light curve. Such a trend has been noted in the literature when attempting to model SNe Ib/c with single-zone models (see, e.g., Maeda et al. 2003 and Valenti et al. 2008) and may indicate that SN 2013ge could be better described by a two-zone model with a high-density inner region and a low-density outer region. Alternatively, this could be evidence for an asymmetry in the explosion.

4. SPECTROSCOPIC PROPERTIES

4.1. Type Ib/c versus Type Iax

SN 2013ge can be immediately identified as an SN I since it lacks *conspicuous* hydrogen emission, and it can further be subclassified as a Type Ib/c from the lack of a strong Si II $\lambda 6355$ feature (Wheeler et al. 1995). Near maximum light, the spectral features are relatively narrow and resemble maximum light spectra of both normal (not broad-lined) SNe Ib/c and Iax (Foley et al. 2013). In order to resolve this degeneracy, in Figure 10 we compare spectra of SN 2013ge

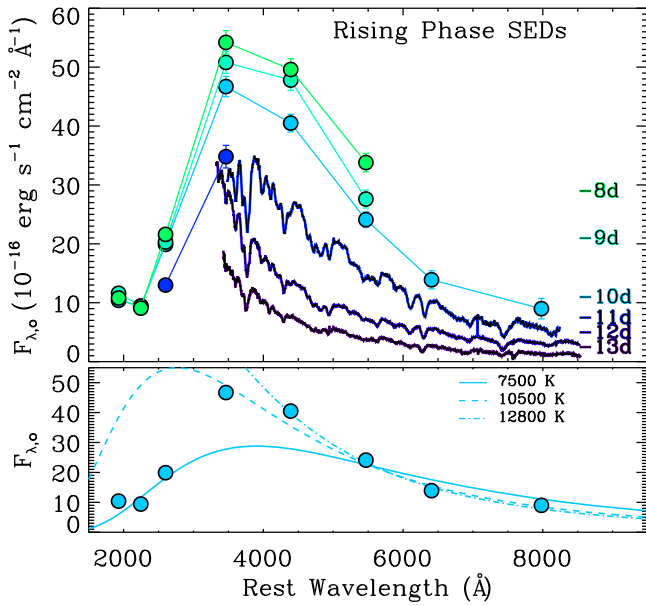


Figure 8. Top: spectra and broadband photometry obtained on the rising phase of the first light curve component. Our earliest spectra, obtained before broadband photometry, show a steep blue continuum with narrow superimposed spectral features. Our first epoch of *Swift*-UVOT photometry (–11 days) constrains the peak of the SED to be around 3500 Å. Early spectra have been multiplied by a constant for clarity. Bottom: –10 day SED with superimposed blackbody fits. It is not possible to fit both the slope of the SED in the optical and the depressed UV flux with a single-temperature blackbody, indicating that line blanketing may be important even at these early epochs.

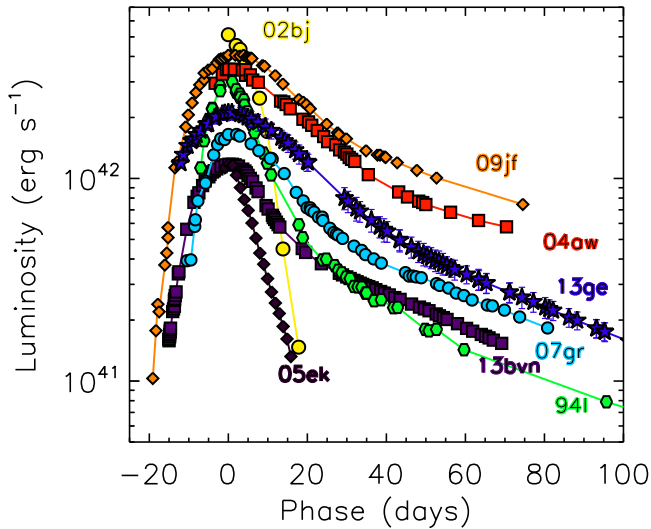


Figure 9. Pseudo-bolometric light curve of SN 2013ge in comparison to other SNe Ib/c. SN 2013ge is relatively faint and slowly evolving. Two distinct peaks are not visible in the pseudo-bolometric light curve, but the morphology of the early UV light curves results in a “shoulder” of excess emission at early times. References for comparison objects: SN 2005ek (Drout et al. 2013), SN 2002bj (Poznanski et al. 2010), SN 2004aw (Taubenberger et al. 2006), SN 2009jf (Valenti et al. 2011), SN 2007gr (Hunter et al. 2009), SN 1994I (Richmond et al. 1996), iPTF13bvn (Fremming et al. 2014). *U*-band photometry was available for all comparison objects with the exception of SN 2002bj. When NIR photometry was available, *UBVR*IJKH data were summed to produce the comparison light curves. When NIR photometry was not available, a blackbody tail was added to an integration of the *UBVR*I data. The comparison light curves shown here do not account for UV flux emitted blueward of the *U* band.

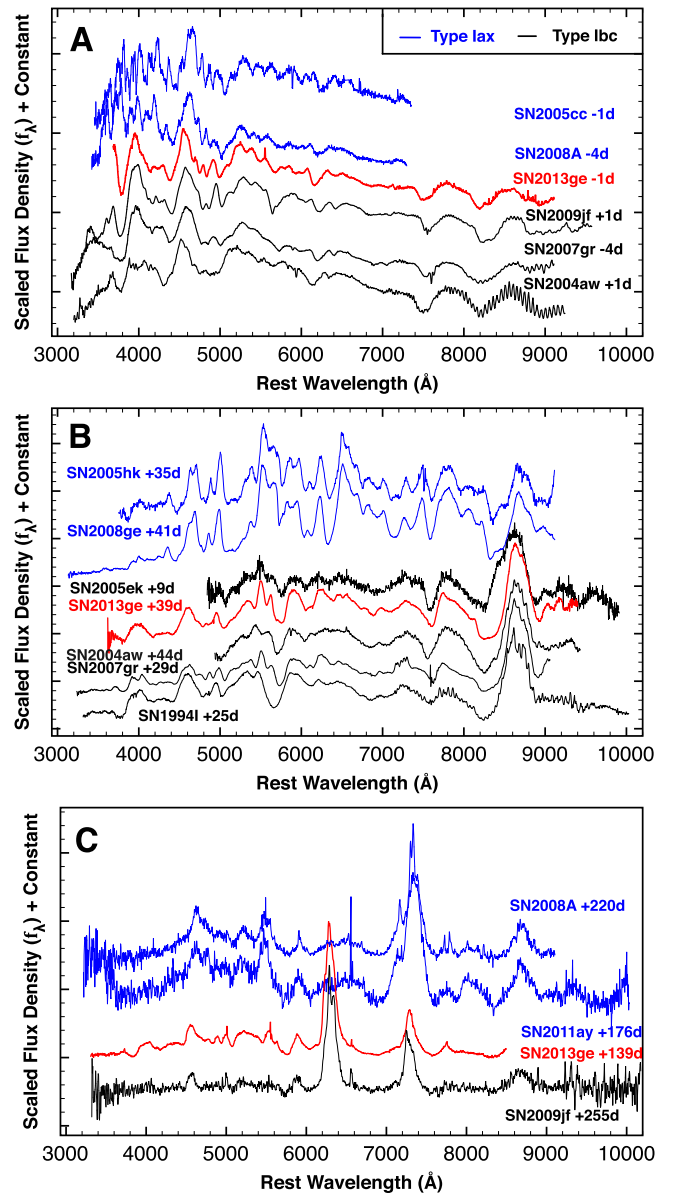


Figure 10. Comparison of the spectrum SN 2013ge at maximum light (panel A), intermediate phases (panel B), and nebular epochs (panel C) to spectra of SNe Ib/c (black) and SNe Iax (blue). Although there is significant overlap between both classes of objects at maximum light, at intermediate and late phases the evolution of SN 2013ge is similar to that of SNe Ib/c. References: SN 2005cc and SN 2008A (Blondin et al. 2012), SN 2005hk (Phillips et al. 2007), SN 2008ge (Silverman et al. 2012), SN 2011ay (Foley et al. 2013), SN 2009jf (Valenti et al. 2011), SN 2007gr (Valenti et al. 2008), SN 2004aw (Taubenberger et al. 2006), SN 2005ek (Drout et al. 2013), SN 1994I (Filippenko et al. 1995).

(red) to spectra of several normal SNe Ib/c (black) and SNe Iax (blue) at three phases: maximum (panel A), intermediate/transitional (panel B), and nebular (panel C).

Taken in conjunction, it is clear that from maximum light onward SN 2013ge follows a spectral evolution typical for normal SNe Ib/c. Near maximum light, iron-peak elements are visible at bluer wavelengths, as well as O I and the Ca II NIR triplet in the red. By +39 days, SN 2013ge has entered a transitional phase, marked by the onset of increased emission in the Ca II NIR triplet. This growth of the Ca II NIR feature has

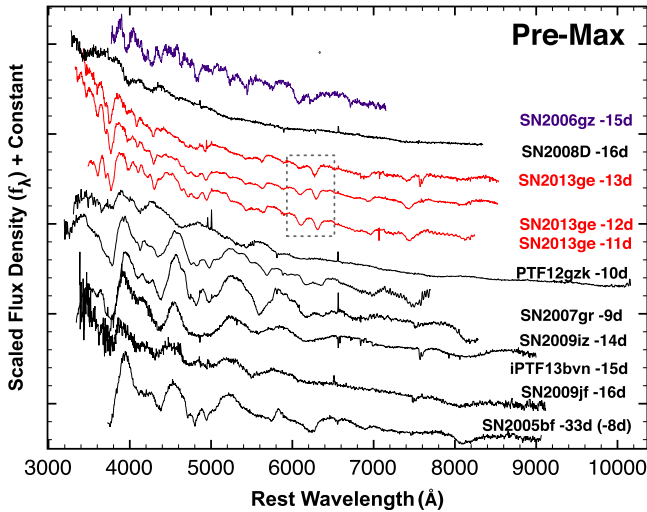


Figure 11. Very early spectra of SN 2013ge (red) compared to other SNe Ib/c (black) and one “super-*Chandra*” SN Ia (purple). The spectra of SN 2013ge are characterized by blue continua and *narrow* spectroscopic features. In contrast, most other SNe Ib/c with spectra at similar epochs show very broad features. One exception is the Type Ib SN 2005bf, which, during its first light curve peak, showed both broad underlying features and narrow high-velocity features of Fe II and Ca II (phases are listed for SN 2005bf with respect to *both* light curve peaks). Interestingly, the “super-*Chandra*” Type Ia SN 2006gz also showed narrow spectroscopic features with blueshifted absorption minima—similar to SN 2013ge—at early times. The dashed gray box highlights two features in the spectra of SN 2013ge whose ratio shows significant evolution over ~ 2 days. References: SN 2006gz (Hicken et al. 2007), SN 2008D (Modjaz et al. 2009), PTF 12gzk (Ben-Ami et al. 2012), SN 2007gr (Valenti et al. 2008), SN 2009iz (Modjaz et al. 2014), iPTF 13bvn (Milisavljevic et al. 2013), SN 2009jf (Sahu et al. 2011), SN 2005bf (Folatelli et al. 2006).

been observed in numerous SNe Ib/c. Finally, at nebular phases SN 2013ge is dominated by emission from forbidden transitions of intermediate-mass elements such as [O I], [Ca II], and Mg I].

This is in stark contrast to SNe Iax, which do not show growth of the Ca II NIR triplet at intermediate phases and whose late-time spectra are dominated by forbidden Ca II and Fe II lines with no obvious contribution from [O I]. However, it is worth emphasizing the strong similarity between some Type Iax spectra and normal Type Ic spectra at maximum light—especially in the wavelength range 4200–7500 Å. The main differentiating spectral features seem to be at wavelengths shorter than 4200 Å, where SNe Iax show a plethora of lines that are not evident in normal SNe Ib/c. Caution should be taken in classifying an SN Iax from a single maximum light spectrum.

4.2. Early Spectra

Despite evolving similarly to normal SNe Ic from maximum onward, the early spectra of SN 2013ge are unusual for SNe Ib/c. Our earliest three spectra, obtained between -13 and -11 days, are characterized by a blue continuum, superimposed with relatively shallow and *narrow* features ($\text{FWHM} \lesssim 3500 \text{ km s}^{-1}$). These spectra were obtained during the early rising phase of the first *u*-band component described in Section 3. Spectroscopic observations of SNe Ib/c at such early epochs are rare, but a majority of events show *broad* high-velocity features at early times, which narrow as the photospheric velocity decreases. Indeed, these spectra vary significantly from the earliest spectra obtained for SN 2008D,

SN 2009jf, PTF 12gzk, and iPTF 13bvn, all of which showed broad spectral features at similar epochs (see Figure 11).

During its first light curve peak, the spectrum of the peculiar Type Ib SN 2005bf did show several narrow spectroscopic features between 4500 and 5300 Å (see Figure 11; phases are given with respect to both the first and second peak). However, features in the rest of the spectrum were broader and more comparable to the other SNe Ib/c shown in Figure 11. Folatelli et al. (2006) interpret this as the combination of an underlying photosphere (broad) and high-velocity iron and calcium features (narrow). In contrast, in the early spectra of SN 2013ge, *all* of the features observed have similarly narrow widths. Intriguingly, the “super-*Chandra*” Type Ia SN 2006gz (Hicken et al. 2007) also showed narrow spectroscopic features with blueshifted absorption minima similar to SN 2013ge at early times. However, by maximum light SN 2006gz developed a very prominent Si II $\lambda 6355$ feature, indicative of SNe Ia, which was not observed in SN 2013ge.

In addition, we observe rapid evolution in both the slope of the continuum and photospheric velocity over the 2 days in which these early spectra of SN 2013ge were obtained. Two absorption features between 6000 and 6500 Å also undergo a large change in their ratio over this time period. These features are highlighted by a gray box in Figure 11.

4.3. Assessing the Presence of Unburned Material

For many models, fully stripping the H/He layers from putative Type Ib/c progenitors has proved challenging. This makes possible identifications of trace amounts of these elements in SNe Ib/c both important and long debated (see Parrent et al. 2014 for a review). Unfortunately, the identification of such contaminants is particularly complicated in the optical photospheric spectra of SNe Ib/c, where a number of degeneracies exist, most notably between H I $\lambda 6563$, C II $\lambda 6580$, and Si II $\lambda 6355$ and between He I $\lambda 5876$ and Na I $\lambda 5889$. These degeneracies can be partially alleviated if NIR spectra are available.

Early phase spectra probe the outermost regions of the ejecta where unburned material such as hydrogen and helium is most likely to be present, if at all. We therefore begin by examining our earliest three optical spectra (days -13 , -12 , -11), as well as our IR spectra at later epochs. In Figure 12 we shift the spectra from rest-frame wavelength to the projected Doppler velocities of commonly found lines in order to examine preliminary matches between spectral features and dominant candidate lines of hydrogen, helium, and carbon. Each panel will be discussed in turn, below.

4.3.1. Hydrogen

When we associate lines with Si II $\lambda 6355$ and Fe II in the left panel of Figure 12, we see that the velocity of the absorption minima is $\sim 14,000 \text{ km s}^{-1}$ (gray vertical bands are placed to guide the eye and correspond to the same velocities in each panel). At the top of the right panel of Figure 12 we show the spectral region around H α (purple). While the feature observed at $\sim 6300 \text{ Å}$ appears at similar velocities to Fe II when interpreted as H α , we find that the velocity overlap and implied velocity evolution are more consistent with the interpretation of C II $\lambda 6580$ (see below for further discussion of carbon). However, this does not preclude very weak contributions from H α to the observed feature.

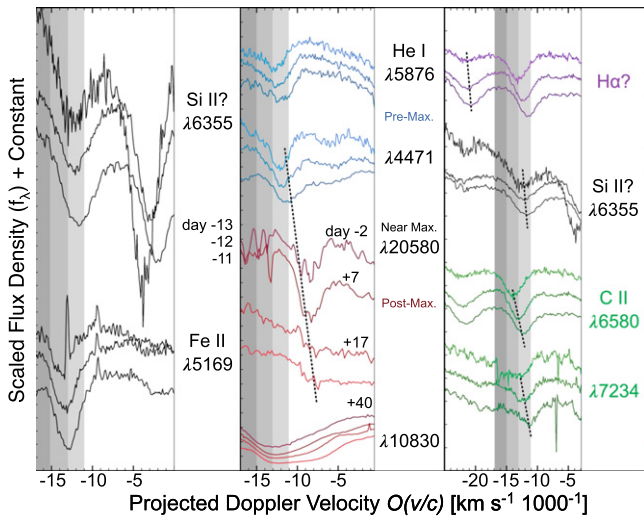


Figure 12. Projected Doppler velocities around key features in the spectra of SN 2013ge. These are used to assess the presence of unburned material (hydrogen, helium, and carbon). Gray regions mark particular velocities and are placed to guide the eye. Dashed lines highlight the velocity evolution of certain features with time. Left: regions around Si II $\lambda 6355$ and Fe II $\lambda 5169$ in the -13 , -12 , and -11 day spectra. Middle: assessing the presence of helium in the early optical spectra (top; blue) and maximum light NIR spectra (bottom; red). See text for details. Right: assessing the degeneracy between H α , Si II $\lambda 6355$, and the presence of C II $\lambda 6580$. See text for details.

We next investigate the possibility of high-velocity H α in these early spectra. In particular, we note that the feature most often associated with Si II $\lambda 6355$ appears at slightly lower velocities than Fe II, which would seem to suggest that photons from deeper layers are escaping opaque resonance line regions of iron. This model-independent discrepancy between the line velocities of Si II and Fe II absorption minima is frequently encountered for SNe Ib/c (e.g., Branch et al. 2006; Elmhamdi et al. 2007; Milisavljevic et al. 2015; see Parrent et al. 2015 for a comprehensive examination) and may indicate that another ion is contributing to the observed line(s). In core-collapse SNe, a candidate line in the wavelength region around Si II $\lambda 6355$ is high-velocity H α (Wheeler et al. 1995; Benetti et al. 2011; Parrent et al. 2015). In the top of the right panel of Figure 12 we show the velocities of Si II (black) versus H I (purple) that would be necessary to overlap with the feature observed at ~ 6100 Å (dashed lines indicate the relevant feature in each case). If H α contributes, it requires velocities in excess of $20,000 \text{ km s}^{-1}$. Unfortunately, we lack certain detections of either Si II $\lambda 5972$ or H β in the early spectra of SN 2013ge, and therefore we cannot definitely confirm the presence or relative contributions of H I versus Si II to the observed feature.

4.3.2. Helium

In the middle panel of Figure 12, we examine the case for He I in the spectra of SN 2013ge. In the top portion of the panel, we show the earliest optical spectra in the region of He I $\lambda\lambda 5876, 4471$ and find evidence for both lines at velocities that are consistent with the composite Fe II feature. A slight notch is also present at ~ 6400 Å, consistent with He I $\lambda 6678$ at a similar velocity (see Figure 14).

In the lower portion of the panel, we examine four NIR spectra (-2 to $+40$ days; red) and focus on the features near 1 and $2 \mu\text{m}$. The large $1 \mu\text{m}$ feature is significantly broader than the $2 \mu\text{m}$ feature and is often attributed to a blend of multiple

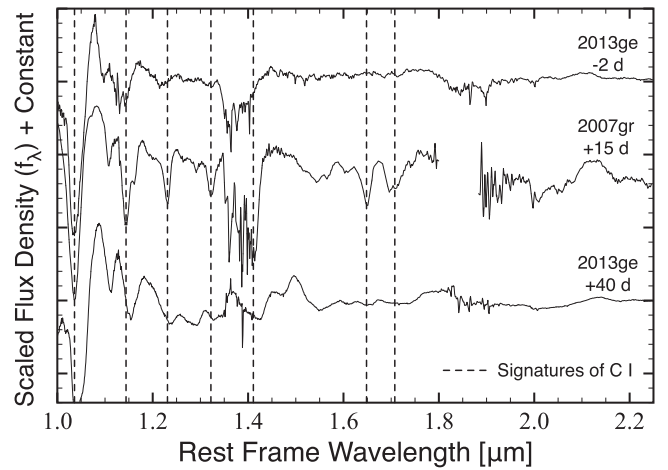


Figure 13. Comparison between the NIR spectra of SN 2007gr and SN 2013ge. Vertical dashed lines denote C I lines marked by Hunter et al. (2009) in their Figure 12. Lines of a comparable strength are not observed in SN 2013ge.

ions including C I and Si I (Millard et al. 1999; Taubenberger et al. 2006). We detect a feature near $2 \mu\text{m}$, which is consistent with faint He I at ~ 8000 – 9000 km s^{-1} . This is comparable to the photospheric velocities at these epochs (the dotted line is placed to guide the eye between the relevant features). Thus, we find that there is room for the existence of He I $\lambda\lambda 4471, 5876, 6678, 10830$, and 20580 in the spectra of SN 2013ge. In addition, the identification of weak optical signatures of He I is consistent with either weak or absent signatures of He I $\lambda\lambda 6678$ and 7065 (Branch et al. 2002; Hachinger et al. 2012).

We therefore conclude that our data are consistent with the identification of weak He I in the early spectra of SN 2013ge. We emphasize that these lines are weak and fade with time; they are distinct from the strong He I features observed in many SNe classified as Type Ib, which are strongest a few weeks past maximum (e.g., Filippenko 1997; Liu et al. 2015). SN 2013ge may therefore represent the detection of weak helium features in an event that would generally be classified as Type Ic.

4.3.3. Carbon

Finally, in the lower portion of the right panel of Figure 12 we identify signatures of C II $\lambda\lambda 6580, 7234$ in the early spectra of SN 2013ge (green). We also examine our NIR spectra for evidence of C I features at later epochs (Figure 13). While we cannot rule out weak contamination from C I, the influence must be substantially weaker than that observed in the NIR spectra of the “carbon-rich” SN 2007gr (Hunter et al. 2009).

4.4. Species Identification and Velocity Estimation

In order to further constrain the full set of ions present in the spectra of SN 2013ge, as well as the evolution of the velocity of the line-forming region, we utilize the fast and publicly available spectral synthesis code SYN++ (Thomas et al. 2011).¹⁹ Line formation in SYN++ is assumed to be dominated by pure resonant scattering with Boltzmann statistics determining relative line strengths for a given ion. We use an exponential optical depth profile that begins at the (sharp)

¹⁹ This is an updated version of SYNOW; <https://c3.lbl.gov/es/>.

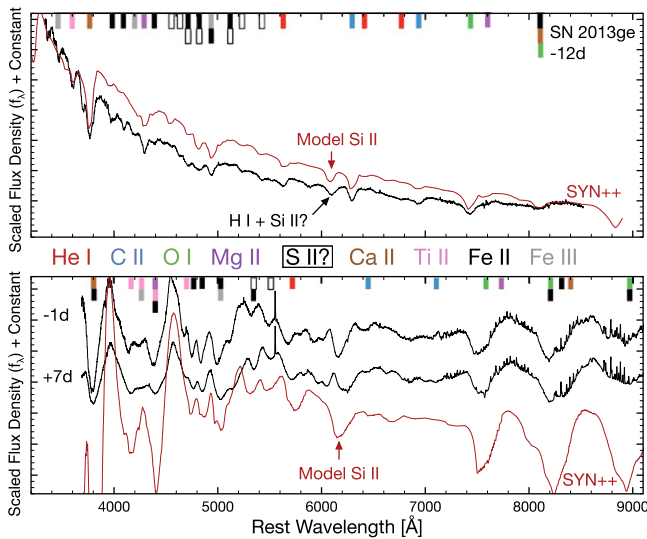


Figure 14. Ion identifications in the early (top panel) and maximum light (bottom panel) spectra of SN 2013ge. Observed spectra are shown in black, while SYN++ models are shown in red. Colored rectangles designate the ions that contribute to each feature in the model spectra, as labeled between the panels. Species identified include He I, C II, and O I, as well as contributions from Mg II, Si II, Ca II, Ti II, Fe II, and possibly S II and Fe III. Between -12 days and maximum light the blue continuum is significantly depressed. See text for more details.

photospheric velocity, which is set by hand for each epoch. See Parrent (2014) for general fitting methods and procedures.

In Figure 14 we present detailed line identifications inferred with SYN++ and show example SYN++ fits (red lines) for both the early phase and maximum light spectra. For the photospheric spectra of SN 2013ge, we tested a full list of ionization species (H I through Fe III). Colored ticks at the top of each panel mark the wavelengths where a given ion is believed to be influencing the spectrum. Main contributors to the model fits include He I, C II, and O I, as well as Mg II, Si II, Ca II, Ti II, Fe II, and possibly S II and Fe III. In the SYN++ models shown, only Si II contributes to the feature observed at ~ 6100 Å (we have not included high-velocity hydrogen).

The velocity of the line-forming region is estimated to decrease from $\sim 15,000$ to $\sim 13,000$ km s $^{-1}$ between -13 and -11 days. This is similar to the early velocity evolution observed in SN 2008D (Modjaz et al. 2009). In order to simultaneously reproduce the relatively high blueshift and narrow width of the features at these early epochs with SYN++, we set the minimum velocity parameter, v_{\min} , for all of the ions to $\sim 15,000$ km s $^{-1}$, while the model photosphere, v_{phot} , was set to $10,000$ km s $^{-1}$. Within the semi-empirical parameter space of SYN++, this is equivalent to the process by which one typically adds “detached” high-velocity features to a spectrum. We emphasize that in this case this process was applied to *all* of the ions and is not necessarily meant to suggest a region that is physically detached from a luminous source; the physical interpretation of these early spectra will be discussed in Section 6.

A similar set of ions is inferred for the maximum light spectrum, although significant evolution is observed. For instance, the spectrum is now significantly redder, a substantial Ti II absorption trough has formed between 4000 and 4500 Å, and the strength of the He I and C II identified features has decreased significantly with respect to the 6250 Å feature (which may be influenced by both Si II $\lambda 6355$ and trace

amounts of hydrogen, as described above). In addition, the velocity of the line-forming region has decreased to $\sim 11,000$ km s $^{-1}$ —typical for SNe Ib/c at maximum light—and the width of the features is relatively well matched to the velocity of their absorption minima. Unfortunately, poor weather prohibited us from obtaining any spectra between -11 and -1 days. As a result, we were unable to observe the evolution from narrow high-velocity features in the early spectra toward moderate width and velocity features in the maximum light spectra.

4.5. Nebular Spectra Analysis

In the left panel of Figure 15 we plot the nebular spectra of SN 2013ge in comparison to SN 2007gr and SN 2009jf. The late-time spectra of SN 2013ge show conspicuous features due to [O I], [Ca II], and Mg I. The flux contained in the [O I] $\lambda\lambda 6300, 6364$ feature is significantly larger than that in either [Ca II] $\lambda\lambda 7291, 7324$ or Mg I $\lambda 4571$, with ratios of ~ 0.3 and ~ 0.12 , respectively. Notably, these ratios show very little evolution between $+150$ and $+450$ days.

The [Ca II]/[O I] ratio may be an indicator of progenitor core mass, with lower values implying a larger core mass, although mixing can also play a role (Fransson & Chevalier 1989). The ratio measured in SN 2013ge is on the low end of values observed in stripped core-collapse SNe, comparable to that observed in SN 2009jf.

Hunter et al. (2009) examined the Mg I/[O I] ratio for a large number of stripped core-collapse SNe, and the ratio observed in SN 2013ge is on the extreme low end when compared to this sample. It is also notable for its lack of evolution; a majority of events show an Mg I/[O I] ratio that grows with time. For example, in SN 2007gr the Mg I/[O I] ratio grows from ~ 0.1 to ~ 1 between 150 and 450 days post-maximum. This growth is *not* observed in either SN 2013ge or SN 2009jf (see Figure 15). To explain a weak Mg I feature at late times in comparison to other SNe, we require either that the abundance of Mg produced in SN 2013ge is lower or that the Mg I line itself is suppressed owing to other effects. For instance, Hunter et al. (2009) invoke mixing in the ejecta to explain the decreasing Mg I/[O I] trend observed in SN 1998bw and SN 2006aj. In addition, in spectral models of SNe IIB, Jerkstrand et al. (2015) find that the Mg I $\lambda 4571$ line is very sensitive to clumping in the O–Ne–Mg layer, with denser clumps favoring brighter emission. In this context, the small Mg I/[O I] ratio observed in SN 2013ge at late times could indicate a relative lack of high-density enhancements due to clumping.

In Figure 15 we plot the [O I] $\lambda\lambda 6300, 6364$ and [Ca II] $\lambda\lambda 7291, 7324$ profiles of SN 2013ge in comparison to those of SN 2004aw and SN 1994I. The shape of the profiles in the $+139$ day spectrum of SN 2013ge appears intermediate between the rounded profiles of SN 1994I and the highly peaked profiles of SN 2004aw, while at $+447$ days the spectrum of SN 2013ge appears more heavily peaked, with slightly blueshifted velocity. Mazzali et al. (2005b) found that a sharp peak in the [O I] feature is consistent with viewing a jet on-axis, although we emphasize that a sharp ejecta density profile can also produce a peaked nebular profile in the absence of a large asymmetry.

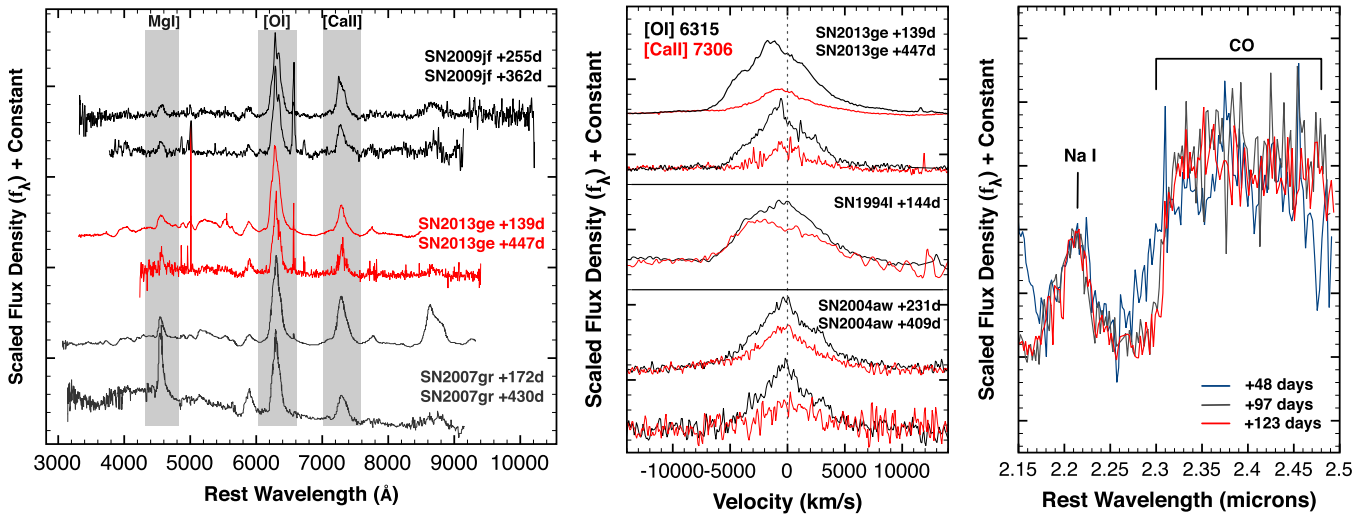


Figure 15. Left: comparison between the nebular spectra of SN 2013ge, SN 2007gr, and SN 2009jf at multiple epochs. At ~ 150 – 250 days, all have a ratio of Mg I $\lambda 4571$ to [O I] $\lambda \lambda 6300, 6364$ of ~ 0.15 . However, by ~ 450 days, the ratio in SN 2007gr has grown substantially to ~ 1 , while it has remained relatively constant in both SN 2013ge and SN 2009jf. Middle: Nebular line profiles of SN 2013ge in comparison to SN 1994I and SN 2004aw at a variety of epochs. By late times the [O I] feature in SN 2013ge more closely resembles the peaked structure observed in SN 2004aw. Right: CO bandhead observed in SN 2013ge at three epochs. We observe evolution of the profile between $+48$ and $+97$ days. References: SN 2009jf (Valenti et al. 2011), SN 2007gr (Chen et al. 2014), SN 2004aw (Taubenberger et al. 2006), SN 1994I (Filippenko et al. 1995).

4.6. The Detection of CO Emission

We identify CO-band emission from the first overtone ($\Delta v = 2$) at $\sim 2.3 \mu\text{m}$ in the NIR spectra of SN 2013ge. Although CO has been detected in the spectra of a number of SNe II, SN 2013ge is only the third SN Ib/c in the literature, to date, with reported molecular CO emission. Previous identifications were reported in SN 2007gr (Hunter et al. 2009) and SN 2000ew (Gerardy et al. 2002). In the right panel of Figure 15 we plot the spectral region between 2.1 and $2.5 \mu\text{m}$ for three epochs of SN 2013ge NIR spectra ($+48$, $+97$, and $+123$ days). The CO bandhead and Na I are labeled. Only marginal emission above the continuum was present in our previous NIR spectrum, indicating significant growth of the CO emission between $+40$ and $+48$ days.

It is also evident that there is evolution of the emission profile between $+48$ and $+97$ days. The feature dramatically narrows, an effect that—to our knowledge—has not previously been observed. The width of the emission feature observed in SN 2007gr did not evolve over a similar range of epochs. This behavior may be linked to different clumping/mixing properties in the ejecta of SN 2013ge and SN 2007gr, as evidenced by their nebular line ratios, above. Detailed modeling of the CO band will be presented in D. Milisavljevic et al. (2016, in preparation).

5. LOCAL ENVIRONMENT PROPERTIES

5.1. Host Galaxy Environment

SN 2013ge exploded on the outskirts of NGC 3287, an SB(s) d galaxy, approximately $51''$ northeast of the galaxy core. This corresponds to an offset—normalized by the g -band half-light radius—of 2.33 . The northeast portion of NGC 3287 is characterized by a large number of blue stellar knots (see Figure 1). In our 2015 January 15 IMACS spectrum the SN flux had fallen enough to reveal an unresolved knot of star formation (in the form of narrow emission lines) at the SN position.

We measured the fluxes of these emission lines at the SN explosion site using the MCMC method of Sanders et al. (2012). The measured $H\alpha$ luminosity of $\sim 1.0 \times 10^{38} \text{ erg s}^{-1}$ leads to an explosion site star formation rate of $\sim 8.0 \times 10^{-4} M_{\odot} \text{ yr}^{-1}$ (Kennicutt 1998). This value is on the low end of the $H II$ regions associated with core-collapse SNe studied by Crowther (2012).

Using the PP04N2 diagnostic (Pettini & Pagel 2004), we find an explosion site metallicity for SN 2013ge of $\log(O/H) + 12 = 8.40 \pm 0.05$. This value is approximately half-solar (assuming $\log(O/H)_{\text{solar}} + 12 = 8.69$; Asplund et al. 2005) and does not deviate strongly from a metallicity measured with an SDSS spectrum taken near the galaxy core. This places the host environment metallicity of SN 2013ge in roughly the bottom 25% of the distribution measured for SNe Ib and Ic and the top 25% measured for Type Ic-BL in Sanders et al. (2012).

5.2. Nonthermal Limits on Progenitor Mass-loss Rate

We observed SN 2013ge in both the radio and X-ray bands during the main part of the optical outburst. Although we obtained only nondetections, these limits are among the deepest ever obtained for an SN Ib/c (Figure 16). Only the nearby ($d \sim 10 \text{ Mpc}$) Type Ic-BL SN 2002ap has intrinsically fainter emission that was detected in both regimes. Particularly notable, our radio observations constrain SN 2013ge to be fainter than SN 2007gr at similar epochs.

For SNe that explode into a relatively low density CSM (as is the case for SNe Ib/c) X-ray emission near maximum light is due to inverse Compton (IC) upscattering of optical photospheric emission by electrons accelerated at the SN shock. In contrast, radio emission is characterized by a synchrotron self-absorbed spectrum, created when the electrons accelerated by the SN shock interact with shock-amplified magnetic fields (Chevalier & Fransson 2006). As such, radio emission and X-ray emission (or lack thereof) provide *independent* constraints on the density of the CSM surrounding the progenitor star.

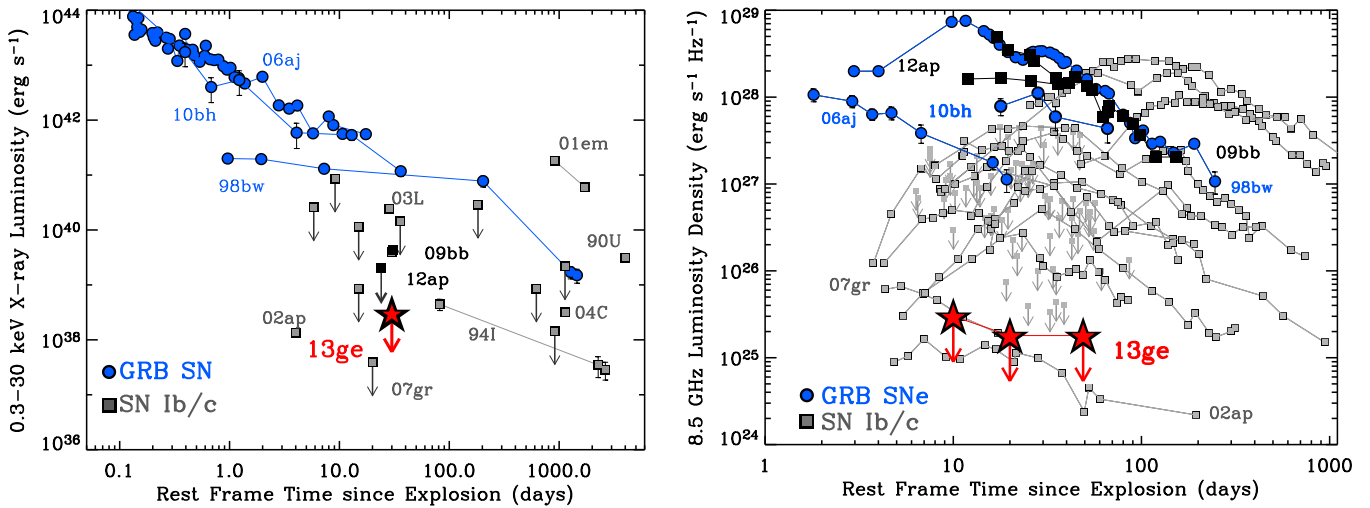


Figure 16. X-ray (left) and radio (right) upper limits obtained for SN 2013ge (red stars) in comparison to other SNe Ib/c. GRB-SNe are shown in blue, relativistic SNe in black, and other SNe Ib/c in gray (labels for notable objects are shown in the same color as the data points). The limits obtained for SN 2013ge are among the deepest to date for an SN Ib/c.

5.2.1. X-Ray IC Limits

To model the X-ray upper limit in the context of IC upscattering, we utilize the models of Margutti et al. (2012, 2014), which are based on the formalism of Chevalier & Fransson (2006). The luminosity of the IC signal is proportional to the bolometric luminosity (L_{bol}) and additionally depends on the outer density structure of the SN ejecta, the density structure of the CSM, the energy spectrum of electrons that upscatter the optical photons, the fraction of post-shock energy in relativistic electrons (ϵ_e), and the explosion properties of the SN (ejecta mass, kinetic energy). The IC signal does *not* depend on the fraction of energy in magnetic fields (ϵ_B), and because $L_{\text{IC}} \propto L_{\text{bol}}$, the mass-loss rate we derive is independent of any uncertainty in the distance to the SN.

Throughout our analysis we use the bolometric light curve derived in Section 3 and assume $M_{\text{ej}} = 2.5 M_{\odot}$ and $E_{\text{K}} = 1.5 \times 10^{51}$ erg. We additionally assume that the accelerated electrons possess a power-law structure of the form $n(\gamma) \propto \gamma^{-p}$ with $p = 3$ (γ is the Lorentz factor of the electrons) and that $\epsilon_e = 0.1$. These values are motivated by the study of SNe Ib/c in the radio (e.g., Chevalier & Fransson 2006; Soderberg et al. 2006c). The outer portion of the SN ejecta is assumed to follow a steep power law of the form $\rho_{\text{SN}} \propto R^{-n}$ with $n = 10$ (e.g., Matzner & McKee 1999). Finally, we consider the case where the density of the CSM can be described as a wind environment with a steady mass-loss rate \dot{M} ($\rho = \dot{M}/4\pi r^2 v_w$, where v_w is the wind velocity). Using these input parameters, our X-ray limit leads to an upper limit on the progenitor mass-loss rate of

$$\dot{M} < 2.3 \times 10^{-5} \left(\frac{v_w}{1000 \text{ km s}^{-1}} \right) M_{\odot} \text{ yr}^{-1}.$$

5.2.2. Radio Synchrotron Limits

To model the radio upper limits in the context of self-absorbed synchrotron emission, we use the models outlined in Kamble et al. (2014), which are based on those of Chevalier (1998). For the radio spectrum characterized by synchrotron self-absorption (SSA), the peak spectral flux (F_{ν_p}) and SSA

frequency (ν_a) are given by

$$F_{\nu_a}(\text{mJy}) = 0.16 A_*^{1.36} \left(\frac{\epsilon_B}{0.1} \right)^{0.64} \left(\frac{\beta}{0.15} \right)^{4.14}$$

$$\nu_a(\text{GHz}) = 6.0 A_*^{0.64} \left(\frac{t}{10 \text{ day}} \right)^{-1.0} \left(\frac{\epsilon_B}{0.1} \right)^{0.36} \left(\frac{\beta}{0.15} \right)^{1.86},$$

where β is the shock velocity in the units of speed of light and A_* is a dimensionless constant used to parameterize the density of the CSM. As described above, for a stellar wind environment, the density surrounding the progenitor star can be parameterized as $\rho = \dot{M}/4\pi r^2 v_w$. Normalizing to a constant mass-loss rate and wind velocity of $\dot{M} = 10^{-5} M_\odot \text{ yr}^{-1}$ and $v_w = 1000 \text{ km s}^{-1}$, respectively, this can further be expressed as $\rho = 5 \times 10^{11} A_* r^{-2} \text{ g cm}^{-3}$ (e.g., $A_* = \left(\frac{\dot{M}}{10^{-5} M_\odot \text{ yr}^{-1}}\right) \left(\frac{v_w}{1000 \text{ km s}^{-1}}\right)^{-1}$). As above, we have also assumed $n(\gamma) \propto \gamma^{-p}$ and $p = 3.0$ for the distribution of relativistic electrons.

Assuming that the shocked material is in equipartition ($\epsilon_e = \epsilon_B$), we can calculate the predicted radio flux for various values of \dot{M} . Each of our radio upper limits places a constraint on the mass-loss rate of the progenitor system. We find that our 3σ upper limit from 9 days post-explosion at 4.8 GHz is the most constraining, leading to an upper limit on the progenitor mass-loss rate of $\dot{M} < 4.0 \times 10^{-6} \left(\frac{v_w}{1000 \text{ km s}^{-1}} \right) \left(\frac{\epsilon_B}{0.1} \right)^{-0.39} M_\odot \text{ yr}^{-1}$. We have scaled to a fiducial value of $\epsilon_B = 0.1$. Combining this with our X-ray limit (which does not depend on ϵ_B), we place the following constraints on the mass loss from the progenitor of SN 2013ge:

$$\dot{M} < 4.0 \times 10^{-6} v_{w,1} \left(\frac{\epsilon_B}{0.1} \right)^{-0.39} M_{\odot} \text{ yr}^{-1} \text{ for } \epsilon_B > 0.001$$

$$\dot{M} < 2.3 \times 10^{-5} v_{\text{w}} M_{\odot} \text{ yr}^{-1} \text{ for } \epsilon_B < 0.001$$

where $v_{w,1}$ is v_w normalized by 1000 km s^{-1} .

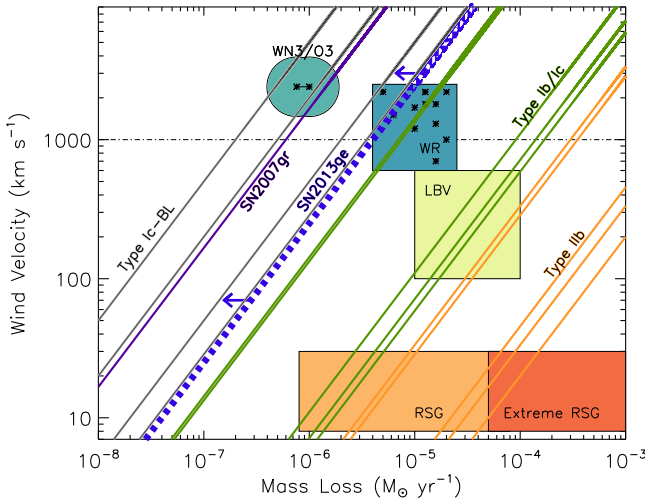


Figure 17. Wind speed vs. mass-loss rate. Locations of galactic W-R stars come from Crowther (2007), WN3/O3 stars from Massey et al. (2015), normal and extreme red supergiants (RSGs) from Marshall et al. (2004), van Loon et al. (2005), and de Jager et al. (1988), and luminous blue variable (LBV) wind (not outburst) properties from Smith (2014). Overplotted are measurements of progenitor mass-loss rate as a function of wind speed for SN 2013ge (this work), SN 2007gr Soderberg et al. (2010), SN 2002ap (Berger et al. 2002), SN 2006aj (Soderberg et al. 2006b), SN 2009bb (Soderberg et al. 2010), SN 2012ap (Chakraborti et al. 2015), SN 1994I (Weiler et al. 2011), SN 1990B (van Dyk et al. 1993), SN 1983N (Sramek et al. 1984), SN 2003L (Soderberg et al. 2005), SN 2008D (Soderberg et al. 2008), SN 2001ig (Ryder et al. 2004), SN 2003bg (Soderberg et al. 2006a), SN 2008ax (Roming et al. 2009), SN 2011dh (Krauss et al. 2012), and SN 2013df (Kamble et al. 2015). We emphasize that the colored boxes represent the wind parameters measured for known, apparently single, evolved massive stars. Binary interaction may play a role in producing the progenitor systems of a significant fraction of stripped SNe.

5.2.3. Comparison to Other Core-collapse SNe

In Figure 17 we plot progenitor mass-loss rate versus wind speed to show how the mass-loss constraints obtained for SN 2013ge compare to those based on radio observations of 15 other stripped-envelope core-collapse SNe (Type IIb, Ib, Ic, and Ic-BL; see caption for references). Radio observations only constrain \dot{M}/v_w , so each SN appears as a diagonal line in this representation. The SNe presented span over four orders of magnitude in \dot{M}/v_w . A horizontal line designates a wind speed of 1000 km s^{-1} , which is often taken as a fiducial value for progenitors of SNe Ib/c. Also shown (colored squares) are regions of this phase space occupied for various classes of (apparently single) evolved massive stars.

In interpreting the data presented in Figure 17, several caveats must be mentioned. First, we plot a single value of \dot{M}/v_w for each SN, representing the CSM at a physical scales of a few $\times 10^{15} \text{ cm}$. Detailed modeling of many Type Ib/c radio light curves reveals a more complex morphology, with some events showing signs of density modulations at larger physical scales or density profiles that vary from the $\rho \propto r^{-2}$ characteristic of a steady wind (Wellons et al. 2012). Similarly, the colored squares represent the locations of known, apparently single, massive stars. How the values of \dot{M} and v_w may change in the final years of a star’s life is an open area of study (e.g., Smith 2014), with mass loss due to binary interaction and eruptive mass-loss events potentially creating complex CSM environments. This is particularly relevant here, as a significant fraction of the observed population of stripped

SNe may have progenitors formed via binary interaction (see, e.g., Smartt 2015, and references therein), although only a small fraction ($\sim 6.5\%$; Margutti et al. 2016) of Type Ib/c progenitors are expected to undergo mass transfer during the final stages of their evolution (“Case-C” mass transfer). Finally, the SNe shown in Figure 17 are events that have been *detected* at radio wavelengths and published in the literature and therefore may be biased toward brighter events.

Nevertheless, despite these caveats, several trends emerge. The SNe IIb all appear at the high end of the CSM density range. They have values of \dot{M}/v_w that intersect with the red/yellow supergiants, as might be expected if their progenitors have not fully lost their hydrogen envelopes.²⁰ Five of the SNe Ib/c fall at intermediate densities, while the SNe Ic-BL appear to preferentially explode in regions of low CSM density. However, it appears that SN 2007gr and SN 2013ge represent examples of *normal* SNe Ib/c that exploded into particularly low density environments, similarly to those observed for the broad-lined (including engine-driven) SNe.

It is possible that this trend is partially due to metallicity. Type Ic-BL events preferentially occur in low-metallicity environments (Sanders et al. 2012), and SN 2013ge and SN 2007gr also occurred in low-metallicity regions of their hosts.²¹ In addition, there are both empirical observations and theoretical predictions (for line-driven or partially line-driven winds) that W-R mass-loss rates are metallicity dependent (Crowther 2007). However, the relativistic²² SN 2009bb and SN 2012ap were both Type Ic-BL events with low CSM densities that occurred in solar or supersolar environments (Levesque et al. 2010; Milisavljevic et al. 2015).

Intriguingly, several SNe Ic-BL and SN 2007gr have measured values of \dot{M}/v_w that are a factor of 3–10 lower than any Galactic or LMC W-R star examined in Crowther (2007). They are consistent with the mass-loss properties inferred for a new class of W-R stars recently discovered in the LMC (Massey et al. 2015). Dubbed WN3/O3, these stars are both fainter in optical bands than “normal” WN/WC stars and have inferred mass-loss rates an order of magnitude lower. The formation mechanism of these new W-R stars is not fully understood, but they demonstrate that some evolved massive stars in the Local Group have mass-loss properties consistent with the very low densities inferred from radio observations of several Type Ic events.

6. DISCUSSION

In this section we discuss the observations outlined above in the context of their implications for the physical configuration of the progenitor system and explosion mechanism of SN 2013ge. From maximum light onward, the optical emission from SN 2013ge is fairly standard for an SN Ib/c. Its explosion parameters ($M_{\text{ej}} = 2\text{--}3 M_{\odot}$, $E_K = (1\text{--}2) \times 10^{51} \text{ erg}$) are well within the range observed for other SNe, and its maximum light

²⁰ The progenitors of several SNe IIb have been identified as yellow supergiants (YGSs) in pre-explosion images (Maund et al. 2004; Elias-Rosa et al. 2009, 2010; Fraser et al. 2010; Van Dyk et al. 2014). The mass-loss rates and wind speeds of YGSs are not well characterized in the literature, but likely fall between RSGs and LBVs.

²¹ The explosion site metallicity of SN 2007gr was $\log(\text{O}/\text{H}) + 12 = 8.5$ (Modjaz et al. 2011), comparable to the LMC.

²² The term “relativistic” SN refers to events whose radio emission reveals a substantial relativistic outflow—likely powered by a central engine—but for which no associated GRB was observed (see Soderberg et al. 2010).

spectra are characterized by ions of various intermediate-mass and iron-peak elements at velocities of $\sim 10,000 \text{ km s}^{-1}$.

However, the early UV and spectroscopic observations of SN 2013ge are unusual. The u -band light curve shows an extra component of emission, which rises on a timescale of ~ 4 – 5 days. During the rising phase of this initial peak, the optical spectra are characterized by a blue continuum superimposed with a plethora of P Cygni features, which are both rapid ($\sim 15,000 \text{ km s}^{-1}$) and narrow (FWHM $\lesssim 3500 \text{ km s}^{-1}$). Below, we discuss the physical interpretation of these early spectra, possible origins for the excess UV emission, and progenitor scenarios that can explain both these observations and the other properties of SN 2013ge.

6.1. Physical Interpretation of the Early Spectra

When an SN shock reaches the low-density outer regions of the progenitor envelope, it will accelerate, leading to a high-velocity gradient in the outer regions of the SN ejecta (Matzner & McKee 1999; Piro & Morozova 2014). The high velocities, rapid velocity evolution, and rapid evolution of observed line ratios in the early spectra of SN 2013ge indicate that we are probing these outer regions. However, for a spherically symmetric explosion in which the differential optical depth of the ejecta decreases monotonically outward from the photosphere, a high-velocity absorption minimum should be accompanied by a broad P Cygni feature. A departure from this picture (as we see in the early spectra of SN 2013ge) implies that the line formation is limited in some sense and likely requires a modification either to the geometry of the explosion or to the optical depth profile of the ejecta.

The high-velocity, narrow absorption features observed in the early spectra of SN 2013ge could be understood in terms of an asymmetric explosion in which a fraction of the ejecta was launched at high velocities along the line of sight to the observer. In this case, the widths of the lines are affected by the opening angle of the ejection. After some time, this material becomes transparent, revealing the underlying photosphere of the bulk explosion. Folatelli et al. (2006) suggest a similar model for the double-peaked SN 2005bf, which displayed both high-velocity Fe II and Ca II lines and broader features (associated with the underlying photosphere) at early times. The presence of both features was understood in terms of the asymmetric explosion being close, but slightly off from the observer angle. In contrast, in SN 2013ge *all* ions observed in the earliest spectra show narrow, high-velocity features; no underlying photosphere with broader components is visible. This has implications for both the ions present in such an asymmetric ejection and the angle at which we observe the outflow.

Alternatively, it may be possible to recreate the spectral features in SN 2013ge if the line absorption coefficient does not decrease monotonically with radius. In this case, the main line-forming region at early epochs could be “detached” above the photosphere. Physically, this could be due to an actual increase in density or to a change in the ionization state of ejecta at a certain distance above the photosphere, resulting in an increased line opacity. The latter argument was used by Tanaka et al. (2009) to explain the high-velocity Ca II and Fe II lines in SN 2005bf. They note that these lines coincide with high-velocity H α , indicating that they were formed in a thin hydrogen shell that remained on the progenitor star at the time of explosion. They argue that the high electron density in this

(solar abundance) hydrogen shell enhances the recombination of Ca III and Fe III (Mazzali et al. 2005b; Tanaka et al. 2009), allowing narrow, high-velocity Ca II and Fe II lines to be formed in the outer portions of the ejecta. In the case of SN 2013ge, a plethora of high-velocity ions are observed at these early epochs, which would have implications for the composition of the outer layers of the progenitor star.

6.2. The Nature of the Early UV Emission

The early rising light curves of SNe I are powered by a combination of two primary sources: energy deposited by the SN shock and the radioactive decay of ^{56}Ni . Excess emission can also be produced by external sources, such as the collision of the SN shock with a binary companion. We now examine the likelihood that the excess UV emission observed in the early light curve of SN 2013ge is powered by each of these sources, as well as the implications for the explosion in each case.

6.2.1. Cooling Envelope Emission

After shock breakout, the shock-heated ejecta cool, giving rise to a light curve component independent from that powered by ^{56}Ni . During this phase, both the bolometric luminosity of the transient and the color temperature should decline with time (Nakar & Sari 2010), with the exact values depending on the radius of the progenitor star, the explosion energy, the ejecta mass, and the ejecta opacity. The luminosity observed in any given optical/UV band will rise as long it is located on the Rayleigh–Jeans tail of the temperature spectrum. As a result, one expects a rise in the UV/optical bands proportional to $t^{1.5}$ if the emission is powered by shock-heated cooling (Nakar & Sari 2010; Piro & Nakar 2013).

In the case of SN 2013ge, the observed rise time for the first u -band component is abnormally large for cooling envelope emission from a stripped progenitor star. A power law of the form $t^{1.5}$ can be fit to the initial rise observed in the u and $w1$ bands (see Figure 5; although this solution is not unique), yielding a rise time of 4–6 days from the epoch of explosion. In contrast, the first light curve components of both SN 2008D and SN 2006aj (which some authors associate with cooling envelope emission; Campana et al. 2006; Soderberg et al. 2008) rise in the UV/optical on timescales $\lesssim 1$ day. By ~ 5 days post-explosion, emission from the radioactive decay of ^{56}Ni likely composes a non-negligible fraction of the total light, making it difficult to assess whether the temperature and luminosity evolution of the first component is consistent with cooling envelope emission. The $u - b$ color remains roughly constant during the rising portion of the first u -band component (before rapidly reddening during the decline phase), which is consistent with the peak of the blackbody passing through the observed band. However, we caution that the UV flux was also depressed compared to a single blackbody during this time period, and the rapid reddening could therefore be due to increased UV line blanketing.

Under the assumption that this emission is caused by shock-heated cooling then, when compared with theoretical models, the long rise time implies that SN 2013ge cannot have a standard W-R progenitor. In order to account for the 4–6 day rise in the u band, we require that the temperature remain above 10^4 K ($\sim 0.9 \text{ eV}$) at a *minimum* for this time period. In contrast, in the W-R model of Nakar & Sari (2010) the temperature has

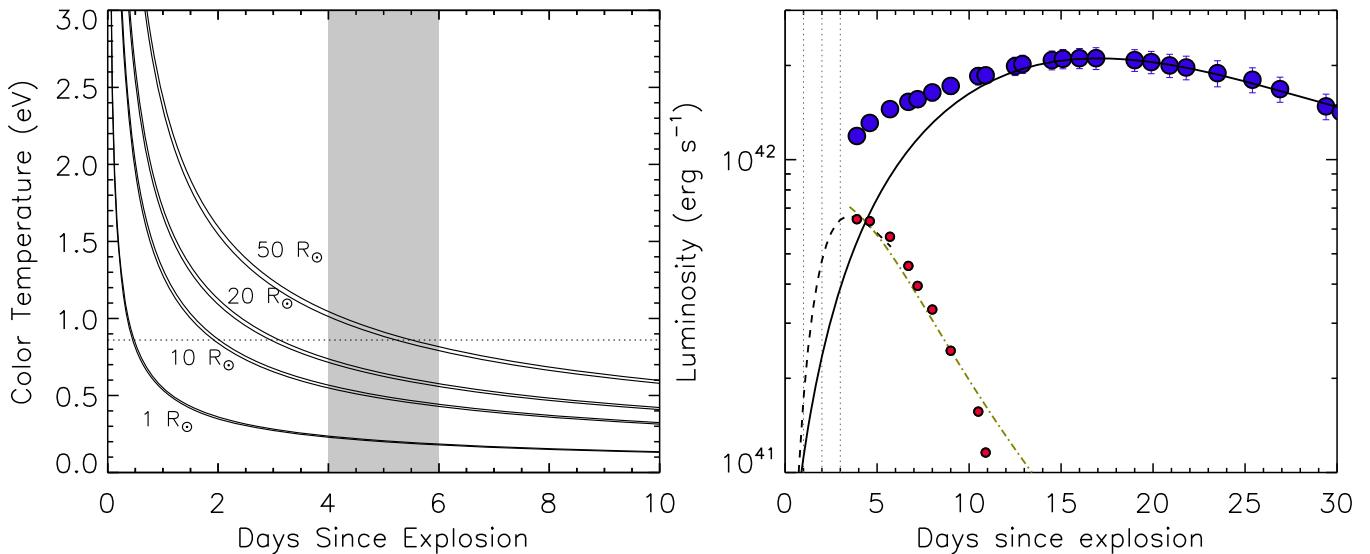


Figure 18. Left: color temperature vs. time since explosion for cooling envelope emission from hydrogen-poor progenitors with radii between 1 and $50 R_{\odot}$. Bands for each radius assume explosion parameters of $M_{\text{ej}} = 2\text{--}3 M_{\odot}$ and $E_K = (1\text{--}2) \times 10^{51}$ erg. If the early emission from SN 2013ge is due to cooling envelope emission, then the temperature must remain above 10,000 K (0.9 eV) at a minimum for 4–6 days post-explosion, implying an extended progenitor. Right: decomposition of the bolometric luminosity of SN 2013ge (blue) into two components. The solid black line represents our best-fit ^{56}Ni decay model to the bulk explosion. Red points show the excess emission above this model at early times. The black dashed line is an Arnett model fit to the rise time and luminosity of this early component, and the gold line is a model for the decline phase based on the instantaneous energy deposition from the $^{56}\text{Ni} \rightarrow ^{56}\text{Co} \rightarrow ^{56}\text{Fe}$ decay chain, allowing for incomplete gamma-ray trapping. Dotted lines indicate the epochs of our early spectra.

already fallen below this level by $\lesssim 1$ day post-explosion. Using the parameterization from Piro & Nakar (2013) for a progenitor with a hydrogen-free radiative envelope, in Figure 18 we plot the color temperature versus time for a range of progenitor radii, assuming $M_{\text{ej}} = 2\text{--}3 M_{\odot}$ and $E_K = (1\text{--}2) \times 10^{51}$ erg (as derived from the bulk explosion). We see that for this envelope structure, we require a progenitor radius of *at least* $50 R_{\odot}$ to account for the observed *u*-band rise. The cooling envelope luminosity at 4 days post-explosion for this model is $(4\text{--}5) \times 10^{41} \text{ erg s}^{-1}$, compatible with the shoulder of excess emission observed at early times.

The modest ejecta mass and extended progenitor radius derived above lead us to also consider the models of Nakar & Piro (2014) for double-peaked SNe. These models employ a nonstandard progenitor envelope structure, in which a massive compact core is surrounded by extended low-mass material. In this picture, the luminosity of the emission is mainly a function of the radius of the extended material, while the time to maximum is related to the total mass in the extended envelope. Both also depend on the velocity and opacity. For a peak time of 4 days, a peak luminosity of $(0.6\text{--}1.2) \times 10^{42} \text{ erg s}^{-1}$, a characteristic velocity of $\sim 12,000 \text{ km s}^{-1}$, and Equations (10) and (12) of Nakar & Piro (2014), we find an extended envelope mass of $\sim 0.1 M_{\odot}$ at a radius of $15\text{--}25 R_{\odot}$. Although less extreme than the value derived for a standard progenitor envelope structure, this is still more extended than a typical W-R progenitor star.

6.2.2. Outwardly Mixed ^{56}Ni

Alternatively, the early emission from SN 2013ge could be due to ^{56}Ni mixed outward in the explosion. In this case, our rising light curve can give constraints on the radial distribution of the outwardly mixed material.

For any given light curve point, there is a degeneracy between the depth of the contributing ^{56}Ni and the explosion

epoch. For deep deposits, there will be a “dark period” between the explosion and the epoch of first light (Piro & Nakar 2013). Our spectroscopic observations from ~ 3 days after the epoch of first light displayed high velocities and rapid velocity evolution, which argue against any significant dark period for SN 2013ge. This is compatible with our first measurement of the luminosity, temperature, and photospheric velocity, which, using Equation (17) of Piro & Nakar (2013), only require that the explosion was ~ 2 days prior to our first bolometric light curve point. In this model, the lack of a significant dark period in SN 2013ge requires that some amount of ^{56}Ni was mixed into the outer portions of the ejecta.

The morphology of the early bolometric light curve also has implications for the distribution of this outwardly mixed ^{56}Ni . A radial distribution of ^{56}Ni that is monotonically decreasing should yield a smoothly rising light curve (e.g., Dessart et al. 2012). In contrast, the “shoulder” of emission as seen in SN 2013ge may require a distinct deposit of ^{56}Ni at shallower depths, qualitatively similar to the model used by Bersten et al. (2013) to explain the first light curve component of SN 2008D. If a small clump of ^{56}Ni -rich material was ejected at high velocities, we can obtain a rough order-of-magnitude estimate for the ejecta mass, nickel mass, and kinetic energy of this material by decomposing the bolometric light curve into two components. This is done in the right panel of Figure 18, where the solid line is our model for the bulk explosion (Section 3) and the red points are the excess above this model at early times.

Using the models of Arnett (1982) to fit the rise time and luminosity of this excess—and assuming a velocity of $\sim 12,000 \text{ km s}^{-1}$ —yields an ejected mass of $\sim 0.06 M_{\odot}$, a ^{56}Ni mass of $\sim 0.012 M_{\odot}$, and a kinetic energy of $\sim 6 \times 10^{49}$ erg. To investigate whether a ^{56}Ni -powered explosion with these parameters is consistent with the rapid post-maximum decline inferred for the early light curve component, we use the model of Drout et al. (2013), which was developed for the

rapidly declining SN 2005ek. It fits the entire post-maximum evolution of an explosion based on the instantaneous rate of energy deposition from the $^{56}\text{Ni} \rightarrow ^{56}\text{Co} \rightarrow ^{56}\text{Fe}$ decay chain, including incomplete trapping of gamma rays produced during $^{56}\text{Ni} \rightarrow ^{56}\text{Co}$ decay. This is appropriate for the declining phase of SNe with very low ejecta masses, which become optically thin quickly, making the models of Arnett (1982) inapplicable.

Using this model with the explosion parameters found above yields the gold curve shown in the right panel of Figure 18, which is well matched to the decline timescale inferred for the early light curve component in SN 2013ge. However, we emphasize that these explosion parameters should be taken as order-of-magnitude estimates only. We do not uniquely decompose the bolometric light curve into multiple components, and the analytical models used here do not account for variations in geometry, opacity, or contributing radioactive species.

6.2.3. Shock Collision with a Binary Companion

Finally, we consider an external source for the early UV emission: a collision between the SN ejecta and a binary companion. During such a collision, a bow shock will form, compressing and shock-heating the SN ejecta in the direction of the interaction. This heating can lead to an extra source of UV/optical emission for several days post-explosion (Kasen 2010). The observed properties of this emission depend on several parameters (e.g., binary separation, ejected mass) and are highly viewing angle dependent. Using a binary population synthesis model for core-collapse SNe, Moriya et al. (2015) find that only $\sim 0.53\%$ of SN Ib/c light curves should have a detectable visible brightening due to this mechanism. As such, any detection of this collision would be rare.

Using the models of Kasen (2010), we assess whether both the luminosity and timescale of the early emission observed in SN 2013ge can be reproduced by this mechanism. Using their Equation (22) and the explosion parameters derived in Section 3, we find that the luminosity of the excess emission in SN 2013ge would require a binary separation of $\lesssim 10^{12}$ cm ($\sim 15 R_\odot$). However, reproducing the timescale of the early emission is challenging. The source of the UV/optical emission in this model is shock-heated cooling, analogous to the cooling envelope emission described above. Thus, in this model, the u -band rise time of 4–6 days similarly requires that the u band remain on the Rayleigh–Jeans tail of the temperature spectrum for this time period. In contrast, none of the models presented in Kasen (2010) have rise times longer than ~ 2 days. Using Equation (15) in Kasen (2010) for the effective temperature of the emission, we find that a separation of at least 10^{13} cm is required to have $T_{\text{eff}} > 10^4$ K at 5 days post-explosion. This is inconsistent with the required separation found above. Thus, we find that (for the current set of theoretical models) the early observations of SN 2013ge are inconsistent with the collision of SN ejecta with a companion star.

6.3. The Progenitor of SN 2013ge

SN 2013ge was the explosion of a stripped massive star with a moderate ejecta mass, *weak* He features in its optical/IR spectra, a low pre-SN mass-loss rate, and a local environment metallicity of ~ 0.5 solar. However, we are left with two distinct scenarios depending on our interpretation of the early emission.

Either SN 2013ge was the explosion of a star with an extended envelope, or it was the result of an explosion in which a clump of ^{56}Ni was mixed outward in the ejecta, possibly coupled to the ejection of a small amount of mass along the line of sight to the observer. We now examine the consistency and consequences of each of these progenitor models. We emphasize that although SN 2013ge is a relatively unique object, the results presented here potentially have general implications for the progenitors of SNe Ib/c. Without either our early spectroscopic observations or early UV coverage, SN 2013ge may not have been flagged as unusual.

6.3.1. Extended Progenitor Surface

If we interpret the early emission from SN 2013ge as cooling envelope emission, it implies that shock breakout occurred from an extended surface. Our estimates for the extent of this surface range from 15–25 R_\odot , for a low-mass envelope on a compact core, to $> 50 R_\odot$ for a standard envelope structure. In principle, this surface either could be a genuinely extended progenitor envelope or could be located within a dense optically thick wind region surrounding the progenitor star.

While some W-R stars have particularly dense wind regions, which extend their photospheric radii by up to a factor of 10 (Li 2007), the interpretation of SN 2013ge as the explosion of such a star is complicated by the need to reconcile it with the radio observations obtained ~ 9 days post-explosion. These observations indicate that by $\sim 10^{15}$ cm (for a standard SN shock velocity of $v_{\text{sh}} = 0.15c$) the progenitor of SN 2013ge is characterized by a low-density wind region. Thus, if the shock breakout occurred within a dense CSM, the progenitor star must have either experienced a significant change in its mass-loss properties or ejected a portion of its envelope during the final stages of its evolution. This process must have occurred within the final $\lesssim 100$ days before core collapse in order to be contained within the region probed by our radio observations or the final $\lesssim 0.5$ days if the breakout radius we derive is the outer extent of this mass. These timescales are normalized to an ejection velocity of 1000 km s^{-1} and are consistent with models that predict that instabilities and internal gravity waves can be induced during the final advanced nuclear burning stages, possibly leading to enhanced mass loss/eruptions during the final year(s) before core collapse (e.g., Shiode & Quataert 2014; Smith & Arnett 2014).

Alternatively, SN 2013ge could be explained by the explosion of a stripped star with a low final mass-loss rate and an inflated stellar envelope. Several of the Type Ib/c binary progenitor models from Yoon et al. (2010) have radii inflated to $\sim 30 R_\odot$, low pre-SN mass-loss rates ($\dot{M} \lesssim 10^{-6} M_\odot \text{ yr}^{-1}$), final masses between 3 and 4 M_\odot (consistent with our derived ejecta masses), and subsolar metallicity. However, the helium envelopes for these progenitors are relatively large ($\sim 1.5 M_\odot$; significantly higher than the mass Hachinger et al. [2012] find is necessary to produce observable features) and are therefore likely inconsistent with the *weak* He I features observed in SN 2013ge. In particular, these low-mass, extended progenitors are predicted to be more efficient at mixing ^{56}Ni into the He-rich layers via Rayleigh–Taylor instabilities (Joggerst et al. 2009; Hammer et al. 2010; Yoon et al. 2010), which should lead to *stronger* observed He lines. Thus, the observations of SN 2013ge likely require a progenitor that differs from any presented in Yoon et al. (2010) in having an extended envelope but *low* final He mass.

Finally, we consider whether this progenitor scenario can account for the unusual spectra observed during the rise of the first light curve component. In particular, while this scenario requires a high effective temperature, the ions present in these spectra are standard singly ionized species. It is possible that this, as well as the unusual velocity profile of the lines, could be understood if there was a change in ionization state in the outer portion of the ejecta, associated with either the low-mass extended envelope or a density enhancement due to a pre-explosion mass ejection. In the former case, the presence of even a very small amount of hydrogen could increase the electron density enough to lead to enhanced recombination (Mazzali et al. 2005a; Tanaka et al. 2008).

6.3.2. Asymmetric Ejection

Alternatively, if we interpret the early emission as heating due to ^{56}Ni , then an asymmetric ejection of a small amount of ^{56}Ni -rich material at high velocities could explain both the early light curve peak and the unusual velocity profile in the early spectra. Intriguingly, our observed velocity ($\sim 15,000 \text{ km s}^{-1}$) and estimated mass ($\sim 0.06 M_{\odot}$) for this material are comparable to those observed in the high-velocity clumps in the northwest portion of the Cassiopeia A (Cas A) SN remnant (Fesen 2001; Hwang et al. 2006). This material in Cas A has an opening angle of $\sim 45^{\circ}$ and has been argued by some to originate in the stellar core (Hwang 2004; Hwang et al. 2006; Milisavljevic & Fesen 2013).

While the moderately peaked nebular emission line profiles and low CSM density observed for SN 2013ge also show similarities to jet-driven explosions in the literature, the observations obtained do not necessarily *require* a highly asymmetric explosion mechanism. They could also potentially be understood if viewing one of the nickel- and silicon-rich plumes of material observed in 3D simulations of mixing instabilities in neutrino-driven explosions (e.g., Hammer et al. 2010). In these models, fast clumps of metal-containing material are able to penetrate through the outer layers of the ejecta, possibly leading to asymmetric variations in the ejecta velocity. Indeed, velocity variations of $\sim 4000 \text{ km s}^{-1}$ were detected in light echoes from the explosion of Cas A, depending on viewing angle (Rest et al. 2011). However, resolved imaging of titanium in Cas A indicates that the explosion mechanism was dominated by slightly asymmetric, low-mode convection, as opposed to a highly asymmetric/bipolar explosion mechanism (Grefenstette et al. 2014).

In this scenario, the weak helium features observed in the spectra of SN 2013ge also have implications for the true helium abundance of the progenitor star. In particular, they suggest a different scenario from that observed in SN 2005bf, where Tanaka et al. (2009) proposed that a ^{56}Ni -rich plume penetrated only slightly into a nearly intact helium envelope. In this case, both the strength and velocity of the observed helium features grew with time as more of the helium envelope fell within a γ -ray optical depth of the ^{56}Ni deposit. In the models of Dessart et al. (2012), the asymmetric ejection of a single blob of ^{56}Ni -rich material to high velocities is only predicted to produce weak helium features. However, if this blob is part of a larger-scale mixing instability, as described above, then it would favor a scenario where the progenitor of SN 2013ge was genuinely He-poor, containing only a thin layer at the time of explosion.

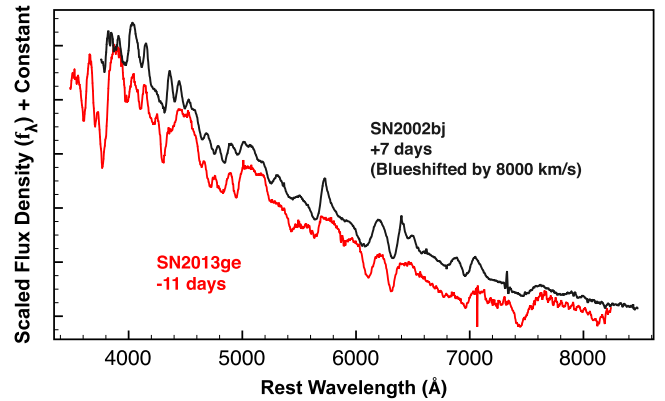


Figure 19. Comparison of an early spectrum of SN 2013ge to a spectrum of the rapidly evolving SN 2002bj (Poznanski et al. 2010). The spectrum of SN 2002bj has been linearly blueshifted by 8000 km s^{-1} .

6.4. Comparison of the Early Emission to the Rapidly Declining SN 2002bj

While investigating the early spectra of SN 2013ge, we found that the first spectrum obtained for the rapidly declining SN 2002bj (Poznanski et al. 2010) displayed a similar blue continuum and narrow spectroscopic features. In Figure 19 we show this spectrum along with the -11 day spectrum of SN 2013ge. The spectrum of SN 2002bj was obtained at $+7$ days, when its photospheric velocity was only $\sim 4000 \text{ km s}^{-1}$, and we have linearly blueshifted it by 8000 km s^{-1} for comparison with SN 2013ge. We emphasize that, unlike in the early spectra of SN 2013ge, there is no mismatch between the widths of the features in this spectrum and the blueshifts of their absorption minima. From modeling its SED as a blackbody, Poznanski et al. (2010) found that the velocity of SN 2002bj was higher at earlier epochs—consistent with a photosphere rapidly receding into a low-mass envelope. Unfortunately, no spectrum of SN 2002bj is available to assess whether its spectroscopic features were similarly narrow at earlier epochs. However, the similarity between the spectrum of SN 2002bj and spectra obtained during the first emission component of SN 2013ge is still striking.

The nature of the explosion that produced SN 2002bj is still a mystery. The rapid light curve and unusual spectrum lead Poznanski et al. (2010) to hypothesize that it was due to the detonation of an He shell on the surface of a WD. Comparing the early emission of SN 2013ge (as shown in Figure 18) to the light curve of SN 2002bj (see Figure 9), we find that the first emission component in SN 2013ge is nearly an order of magnitude fainter and also declines a factor of ~ 1.4 faster than the bolometric light curve of SN 2002bj. Thus, even neglecting the second (main) light curve component of SN 2013ge (which is entirely lacking in SN 2002bj), the energetics of these explosions are very different. However, Figure 19 demonstrates that the ions and ionization state present in the ejecta of SN 2002bj can also be produced during the core collapse of a massive star. It has already been shown that massive stars may be able to produce rapidly evolving SNe I, either owing to very low ejecta masses (Drout et al. 2013; Tauris et al. 2013) or through the combination of a large progenitor radius and a lack of ejected radioactive elements (Kleiser & Kasen 2014). More detailed modeling attempting to ascertain whether SN 2002bj may be a more extreme example of the first emission component in SN 2013ge in an explosion that lacks the second,

main, light curve component powered by ^{56}Ni would be warranted.

7. SUMMARY AND CONCLUSIONS

We have presented extensive observations of the Type Ib/c SN 2013ge beginning ~ 2 days post-explosion, when the light curve is particularly sensitive to both the progenitor configuration and mixing within the ejecta. Here we summarize our main conclusions.

Early Emission: The rapid velocity evolution and rapid rise observed in the early spectra and UV light curves, respectively, indicate that our first observations probe the outer regions of the ejecta shortly after explosion. The early u -band and UV light curves show two distinct components. The first component has a rise time of ~ 4 – 5 days and is visible for the first week post-explosion. This manifests itself as a “shoulder” of excess emission in the bolometric light curve with a luminosity of $\sim 6 \times 10^{41} \text{ erg s}^{-1}$. Spectra of the first component display a blue continuum and are unusual in possessing features that are both moderately high velocity ($\sim 15,000 \text{ km s}^{-1}$) and narrow ($\sim 3500 \text{ km s}^{-1}$). This indicates that the line formation region is limited in some sense, possibly owing to an asymmetric geometry or a change in ionization state in the outer portions of the ejecta.

Bulk Explosion: With $M_{\text{R,peak}} = -17.5$ and $\Delta m_{15,R} = 0.4$, SN 2013ge is relatively faint and slowly evolving, but the derived ejecta mass (2 – $3 M_{\odot}$) and kinetic energy ($(1$ – $2) \times 10^{51} \text{ erg}$) are well within the distribution observed for SNe Ib/c. Weak He I lines, which fade with time, are detected in early optical and NIR spectra. These are distinct from the conspicuous He I lines that are usually used to classify SNe Ib. Near maximum light the spectra are dominated by a plethora of intermediate-mass and iron-peak elements. The late-time spectral evolution of SN 2013ge is also distinctive, showing a lack of evolution in the $\text{Mg I}/[\text{O I}]$ ratio and a shifting CO-emission profile.

Environment Properties: SN 2013ge exploded on the outskirts of a star-forming galaxy. There is an unresolved H II region at the explosion site, which has a metallicity of ~ 0.5 solar. The radio and X-ray limits for SN 2013ge are among the deepest ever obtained for a stripped-envelope SN and constrain the progenitor mass-loss rate to be $\dot{M} < 4.0 \times 10^{-6} M_{\odot} \text{ yr}^{-1}$ for $\epsilon_B = 0.1$.

Power Sources and Progenitors: SN 2013ge was the explosion of a stripped massive star with a moderate ejecta mass. However, we are left with two distinct progenitor scenarios depending on our interpretation of the early emission. In both cases, we find it likely that the progenitor of SN 2013ge had only a thin layer of helium remaining at the time of core collapse.

1. If the early emission is due to post-shock-breakout cooling envelope emission, then its relatively long rise time (~ 4 – 6 days) requires either that the progenitor of SN 2013ge had an extended envelope or that it ejected a small portion of its envelope in the final $\lesssim 1$ yr before core collapse.
2. If the early emission is due to outwardly mixed ^{56}Ni , then we require that a distinct clump of ^{56}Ni was mixed into the very outer portions of the ejecta. Coupled with the early spectra, this may imply an asymmetric ejection of a small amount of nickel-rich material at high velocities.

More detailed modeling beyond the scope of this work will be necessary to fully distinguish between or rule out one of these two progenitor scenarios. In particular, it would be useful to ascertain whether either scenario can actually reproduce the plethora of high-velocity and narrow features observed in the early spectra, with the cooling envelope model facing the additional challenge of explaining the depressed UV flux at early epochs. We note that if the epoch of first light is earlier than that derived in Section 3 from power-law fits to the early UV light curves, then the cooling envelope/extended progenitor scenario would be put under additional tension, or ruled out entirely. In contrast, the model of a high-velocity clump could be naturally extended to explain a rise in the UV light curve after the epoch of first light. Finally, we find that current theoretical models for the collision of an SN shock with a binary companion cannot reproduce both the luminosity and timescale of the early emission observed in SN 2013ge.

Rapidly Evolving SN 2002bj: The early spectra of SN 2013ge are similar to the spectrum of the rapidly evolving SN 2002bj, demonstrating that the ions and ionization state present in the ejecta of SN 2002bj can also be produced by the core collapse of a massive star.

We thank the anonymous referee for numerous comments that improved this manuscript. M.R.D. thanks L. Z. Kelley, D. Kasen, and E. Ramirez-Ruiz for useful discussions. We thank N. Morrell for obtaining some of the observations reported here. M.R.D. is supported in part by the NSF Graduate Research Fellowship. M.L.G.’s position in the supernova research group at UC Berkeley is supported by Gary and Cynthia Bengier and NSF grant AST-1211916. E.Y.H. acknowledges the generous support provided by the Danish Agency for Science and Technology and Innovation through a Sapere Aude Level 2 grant.

This paper includes data gathered with the 6.5 m *Magellan* Telescopes located at Las Campanas Observatory, Chile. Some observations reported here were obtained at the MMT observatory, a joint facility of the Smithsonian Institution and the University of Arizona. This paper uses data taken with the MODS spectrographs built with funding from NSF grant AST-9987045 and the NSF Telescope System Instrumentation Program (TSIP), with additional funds from the Ohio Board of Regents and the Ohio State University Office of Research.

Facilities: *Swift* (UVOT), *Magellan*: Baade (IMACS, FIRE), *Magellan*: Clay (LDSS3), MMT (Blue Channel spectrograph, Hectospec, MMTcam), LBT (MODS), FLWO: L2m (FAST, KeplerCam), *Chandra*, VLA, Shane (Kast), Hiltner (OSMOS).

REFERENCES

- Allington-Smith, J., Breare, M., Ellis, R., et al. 1994, *PASP*, **106**, 983
 Arcavi, I., Gal-Yam, A., Yaron, O., et al. 2011, *ApJL*, **742**, L18
 Arnett, W. D. 1982, *ApJ*, **253**, 785
 Asplund, M., Grevesse, N., & Sauval, A. J. 2005, in ASP Conf. Ser. 336, Cosmic Abundances as Records of Stellar Evolution and Nucleosynthesis, ed. T. G. Barnes, III, & F. N. Bash (San Francisco, CA: ASP), 25
 Begelman, M. C., & Sarazin, C. L. 1986, *ApJL*, **302**, L59
 Ben-Ami, S., Gal-Yam, A., Filippenko, A. V., et al. 2012, *ApJL*, **760**, L33
 Benetti, S., Turatto, M., Valenti, S., et al. 2011, *MNRAS*, **411**, 2726
 Berger, E., Kulkarni, S. R., & Chevalier, R. A. 2002, *ApJL*, **577**, L5
 Bersten, M. C., Benvenuto, O. G., Nomoto, K., et al. 2012, *ApJ*, **757**, 31
 Bersten, M. C., Tanaka, M., Tominaga, N., Benvenuto, O. G., & Nomoto, K. 2013, *ApJ*, **767**, 143
 Blondin, S., Matheson, T., Kirshner, R. P., et al. 2012, *AJ*, **143**, 126
 Branch, D., Benetti, S., Kasen, D., et al. 2002, *ApJ*, **566**, 1005
 Branch, D., Jeffery, D. J., Young, T. R., & Baron, E. 2006, *PASP*, **118**, 791

- Breeveld, A. A., Landsman, W., Holland, S. T., et al. 2011, in AIP Con. Ser. 1358, ed. J. E. McEnery, J. L. Racusin, & N. Gehrels (Melville, NY: AIP), 373
- Brown, P. J., Holland, S. T., Immler, S., et al. 2009, *AJ*, 137, 4517
- Burrows, A., Dessart, L., Livne, E., Ott, C. D., & Murphy, J. 2007, *ApJ*, 664, 416
- Campana, S., Mangano, V., Blustin, A. J., et al. 2006, *Natur*, 442, 1008
- Cao, Y., Kasliwal, M. M., Arcavi, I., et al. 2013, *ApJL*, 775, L7
- Chakraborti, S., Soderberg, A., Chomiuk, L., et al. 2015, *ApJ*, 805, 187
- Chen, J., Wang, X., Ganeshalingam, M., et al. 2014, *ApJ*, 790, 120
- Chevalier, R. A. 1998, *ApJ*, 499, 810
- Chevalier, R. A., & Fransson, C. 2006, *ApJ*, 651, 381
- Corsi, a., Ofek, E. O., Gal-Yam, a., et al. 2012, *ApJL*, 747, L5
- Crowther, P. A. 2007, *ARA&A*, 45, 177
- Crowther, P. A. 2012, *MNRAS*, 428, 1927
- de Jager, C., Nieuwenhuijzen, H., & van der Hucht, K. A. 1988, *A&AS*, 72, 259
- Dessart, L., Hillier, D. J., Li, C., & Woosley, S. 2012, *MNRAS*, 424, 2139
- Dressler, A., Hare, T., Bigelow, B. C., & Osip, D. J. 2006, *Proc. SPIE*, 6269, 62690F
- Drout, M. R., Soderberg, A. M., Gal-Yam, A., et al. 2011, *ApJ*, 741, 97
- Drout, M. R., Soderberg, A. M., Mazzali, P. A., et al. 2013, *ApJ*, 774, 58
- Elias-Rosa, N., Van Dyk, S. D., Li, W., et al. 2009, *ApJ*, 706, 1174
- Elias-Rosa, N., Van Dyk, S. D., Li, W., et al. 2010, *ApJL*, 714, L254
- Elmhamdi, A., Danziger, I. J., Branch, D., & Leibundgut, B. 2007, in AIP Conf. Ser. 924, The Multicolored Landscape of Compact Objects and Their Explosive Origins, ed. T. di Salvo et al. (San Francisco, CA: ASP), 277
- Fabricant, D., Cheimets, P., Caldwell, N., & Geary, J. 1998, *PASP*, 110, 79
- Fabricant, D., Fata, R., Roll, J., et al. 2005, *PASP*, 117, 1411
- Fesen, R. A. 2001, *ApJS*, 133, 161
- Filippenko, A. V. 1997, *ARA&A*, 35, 309
- Filippenko, A. V., Barth, A. J., Matheson, T., et al. 1995, *ApJL*, 450, L11
- Folatelli, G., Contreras, C., Phillips, M. M., et al. 2006, *ApJ*, 641, 1039
- Foley, R. J., Challis, P. J., Chornock, R., et al. 2013, *ApJ*, 767, 57
- Fransson, C., & Chevalier, R. A. 1989, *ApJ*, 343, 323
- Fraser, M., Takáts, K., Pastorello, A., et al. 2010, *ApJL*, 714, L280
- Fremling, C., Sollerman, J., Taddia, F., et al. 2014, *A&A*, 565, A114
- Gehrels, N., Chincarini, G., Giommi, P., et al. 2004, *ApJ*, 611, 1005
- Gerardy, C. L., Fesen, R. A., Nomoto, K., et al. 2002, *PASP*, 54, 905
- Gorbikov, E., Gal-Yam, A., Ofek, E. O., et al. 2014, *MNRAS*, 443, 671
- Grefenstette, B. W., Harrison, F. A., Boggs, S. E., et al. 2014, *Natur*, 506, 339
- Hachinger, S., Mazzali, P. a., Taubenberger, S., et al. 2012, *MNRAS*, 422, 70
- Hammer, N. J., Janka, H.-T., & Müller, E. 2010, *ApJ*, 714, 1371
- Hicken, M., Challis, P., Kirshner, R. P., et al. 2012, *ApJS*, 200, 12
- Hicken, M., Garnavich, P. M., Prieto, J. L., et al. 2007, *ApJL*, 669, L17
- Hsiao, E. Y., Burns, C. R., Contreras, C., et al. 2015, *A&A*, 578, A9
- Hunter, D. J., Valenti, S., Kotak, R., et al. 2009, *A&A*, 508, 371
- Hwang, U., Laming, J. M., Badenes, C., et al. 2004, *ApJL*, 615, L117
- Jerkstrand, A., Ergon, M., Smartt, S. J., et al. 2015, *A&A*, 573, A12
- Joggerst, C. C., Woosley, S. E., & Heger, A. 2009, *ApJ*, 693, 1780
- Kalberla, P. M. W., Burton, W. B., Hartmann, D., et al. 2005, *A&A*, 440, 775
- Kamble, A., Margutti, R., Soderberg, A. M., et al. 2015, *ApJ*, 818, 111
- Kamble, A., Soderberg, A. M., Chomiuk, L., et al. 2014, *ApJ*, 797, 2
- Kasen, D. 2010, *ApJ*, 708, 1025
- Kennicutt, R. C. 1998, *ARA&A*, 36, 189
- Kifonidis, K., Plewa, T., Scheck, L., Janka, H.-T., & Müller, E. 2006, *A&A*, 453, 661
- Kleiser, I. K. W., & Kasen, D. 2014, *MNRAS*, 438, 318
- Krauss, M. I., Soderberg, A. M., Chomiuk, L., et al. 2012, *ApJL*, 750, L40
- Laming, J. M., Hwang, U., Radics, B., Lekli, G., & Takács, E. 2006, *ApJ*, 644, 260
- Landolt, A. U. 1992, *AJ*, 104, 340
- Levesque, E. M., Soderberg, a. M., Foley, R. J., et al. 2010, *ApJL*, 709, L26
- Li, L.-X. 2007, *MNRAS*, 375, 240
- Liu, Y.-Q., Modjaz, M., Bianco, F. B., & Graur, O. 2015, arXiv:1510.08049
- Lucy, L. B. 1991, *ApJ*, 383, 308
- Lyman, J., Bersier, D., James, P., et al. 2014, *MNRAS*, 437, 3848
- Maeda, K., Mazzali, P. A., Deng, J., et al. 2003, *ApJ*, 593, 931
- Maeda, K., Nakamura, T., Nomoto, K., et al. 2002, *ApJ*, 565, 405
- Maeda, K., Tanaka, M., Nomoto, K., et al. 2007, *ApJ*, 666, 1069
- Marek, A., & Janka, H.-T. 2009, *ApJ*, 694, 664
- Margutti, R., Guidorzi, C., Lazzati, D., et al. 2015, *ApJ*, 805, 159
- Margutti, R., Kamble, A., Milisavljevic, D., et al. 2016, arXiv:1601.06806
- Margutti, R., Parrent, J., Kamble, A., et al. 2014, *ApJ*, 790, 52
- Margutti, R., Soderberg, A. M., Chomiuk, L., et al. 2012, *ApJ*, 751, 134
- Marshall, J. R., van Loon, J. T., Matsuura, M., et al. 2004, *MNRAS*, 355, 1348
- Martini, P., Stoll, R., Derwent, M. A., et al. 2011, *PASP*, 123, 187
- Massey, P., Neugent, K. F., Morrell, N., & John Hillier, D. 2015, in IAU Symp. 307, New Windows on Massive Stars: Asteroseismology, Interferometry, and Spectropolarimetry (Cambridge: Cambridge Univ. Press), 64
- Matheson, T., Kirshner, R. P., Challis, P., et al. 2008, *AJ*, 135, 1598
- Matzner, C. D., & McKee, C. F. 1999, *ApJ*, 510, 379
- Maud, J. R., Smartt, S. J., Kudritzki, R. P., Podsiadlowski, P., & Gilmore, G. F. 2004, *Natur*, 427, 129
- Mazzali, P. A., Benetti, S., Stehle, M., et al. 2005a, *MNRAS*, 357, 200
- Mazzali, P. A., Kawabata, K. S., Maeda, K., et al. 2005b, *Sci*, 308, 1284
- Mazzali, P. A., Valenti, S., Della Valle, M., et al. 2008, *Sci*, 321, 1185
- Milisavljevic, D., Fesen, R., Pickering, T., et al. 2013, *ATel*, 5142, 1
- Milisavljevic, D., & Fesen, R. A. 2013, *ApJ*, 772, 134
- Milisavljevic, D., Margutti, R., Parrent, J. T., et al. 2015, *ApJ*, 799, 51
- Millard, J., Branch, D., Baron, E., et al. 1999, *ApJ*, 527, 746
- Miller, J. S., & Stone, R. P. S. 1993, Lick Observatory Tech. Rep. 66 (Santa Cruz, CA: Lick Obs.)
- Modjaz, M., Blondin, S., Kirshner, R. P., et al. 2014, *AJ*, 147, 99
- Modjaz, M., Kewley, L., Bloom, J. S., et al. 2011, *ApJL*, 731, L4
- Modjaz, M., Li, W., Butler, N., et al. 2009, *ApJ*, 702, 226
- Moriya, T. J., Liu, Z.-W., & Izzard, R. G. 2015, *MNRAS*, 450, 3264
- Mould, J. R., Huchra, J. P., Freedman, W. L., et al. 2000, *ApJ*, 529, 786
- Nakar, E. 2015, *ApJ*, 807, 172
- Nakar, E., & Piro, A. L. 2014, *ApJ*, 788, 193
- Nakar, E., & Sari, R. 2010, *ApJ*, 725, 904
- Nugent, P. E., Sullivan, M., Cenko, S. B., et al. 2011, *Natur*, 480, 344
- Parrent, J., Friesen, B., & Parthasarathy, M. 2014, *Ap&SS*, 351, 1
- Parrent, J. T. 2014, arXiv:1412.7163
- Parrent, J. T., Milisavljevic, D., Soderberg, A. M., & Parthasarathy, M. 2015, arXiv:1505.06645
- Pastorello, a., Kasliwal, M. M., Crockett, R. M., et al. 2008, *MNRAS*, 389, 955
- Pettini, M., & Pagel, B. E. J. 2004, *MNRAS*, 348, L59
- Phillips, M. M., Li, W., Frieman, J. A., et al. 2007, *PASP*, 119, 360
- Piro, A. L., & Morozova, V. S. 2014, *ApJL*, 792, L11
- Piro, A. L., & Nakar, E. 2013, *ApJ*, 769, 67
- Podsiadlowski, P., Joss, P. C., & Hsu, J. J. L. 1992, *ApJ*, 391, 246
- Pogge, R. W., Atwood, B., Brewer, D. F., et al. 2010, *Proc. SPIE*, 7735, 77350
- Poznanski, D., Chornock, R., Nugent, P. E., et al. 2010, *Sci*, 327, 58
- Poznanski, D., Prochaska, J. X., & Bloom, J. S. 2012, *MNRAS*, 426, 1465
- Rabinak, I., & Waxman, E. 2011, *ApJ*, 728, 63
- Rest, A., Foley, R. J., Sinnott, B., et al. 2011, *ApJ*, 732, 3
- Richmond, M. W., van Dyk, S. D., Ho, W., et al. 1996, *AJ*, 111, 327
- Roming, P. W. A., Kennedy, T. E., Mason, K. O., et al. 2005, *SSRv*, 120, 95
- Roming, P. W. A., Pritchard, T. A., Brown, P. J., et al. 2009, *ApJL*, 704, L118
- Ryder, S. D., Sadler, E. M., Subrahmanyam, R., et al. 2004, *MNRAS*, 349, 1093
- Sahu, D. K., Gurugubelli, U. K., Anupama, G. C., & Nomoto, K. 2011, *MNRAS*, 413, 2583
- Sanders, N. E., Soderberg, a. M., Levesque, E. M., et al. 2012, *ApJ*, 758, 132
- Scheck, L., Kifonidis, K., Janka, H.-T., & Müller, E. 2006, *A&A*, 457, 963
- Schlaflly, E. F., & Finkbeiner, D. P. 2011, *ApJ*, 737, 103
- Schmidt, G. D., Weymann, R. J., & Foltz, C. B. 1989, *PASP*, 101, 713
- Shiode, J. H., & Quataert, E. 2014, *ApJ*, 780, 96
- Silverman, J. M., Foley, R. J., Filippenko, A. V., et al. 2012, *MNRAS*, 425, 1789
- Simcoe, R. A., Burgasser, A. J., Schechter, P. L., et al. 2013, *PASP*, 125, 270
- Smartt, S. J. 2015, *PASA*, 32, e016
- Smith, J. A., Tucker, D. L., Kent, S., et al. 2002, *AJ*, 123, 2121
- Smith, N. 2014, *ARA&A*, 52, 487
- Smith, N., & Arnett, W. D. 2014, *ApJ*, 785, 82
- Soderberg, a. M., Berger, E., Page, K. L., et al. 2008, *Natur*, 453, 469
- Soderberg, a. M., Brunthaler, a., Nakar, E., Chevalier, R. a., & Bietenholz, M. F. 2010, *ApJ*, 725, 922
- Soderberg, A. M., Chakraborti, S., Pignata, G., et al. 2010, *Natur*, 463, 513
- Soderberg, A. M., Chevalier, R. A., Kulkarni, S. R., & Frail, D. A. 2006a, *ApJ*, 651, 1005
- Soderberg, A. M., Kulkarni, S. R., Berger, E., et al. 2005, *ApJ*, 621, 908
- Soderberg, A. M., Kulkarni, S. R., Nakar, E., et al. 2006b, *Natur*, 442, 1014
- Soderberg, A. M., Nakar, E., Berger, E., & Kulkarni, S. R. 2006c, *ApJ*, 638, 930
- Speziali, R., Di Paola, A., Giallongo, E., et al. 2008, *Proc. SPIE*, 7014, 70144
- Sramek, R. A., Panagia, N., & Weiler, K. W. 1984, *ApJL*, 285, L59
- Tanaka, M., Kawabata, K. S., Maeda, K., et al. 2009, *ApJ*, 699, 1119
- Tanaka, M., Mazzali, P. A., Benetti, S., et al. 2008, *ApJ*, 677, 448

- Taubenberger, S., Pastorello, A., Mazzali, P. a., et al. 2006, [MNRAS](#), **371**, 1459
- Tauris, T. M., Langer, N., Moriya, T. J., et al. 2013, [ApJL](#), **778**, L23
- Thomas, R. C., Nugent, P. E., & Meza, J. C. 2011, [PASP](#), **123**, 237
- Vacca, W. D., Cushing, M. C., & Rayner, J. T. 2003, [PASP](#), **115**, 389
- Valenti, S., Elias-Rosa, N., Taubenberger, S., et al. 2008, [ApJL](#), **673**, L155
- Valenti, S., Fraser, M., Benetti, S., et al. 2011, [MNRAS](#), **416**, 3138
- van Dyk, S. D., Sramek, R. A., Weiler, K. W., & Panagia, N. 1993, [ApJ](#), **409**, 162
- Van Dyk, S. D., Zheng, W., Fox, O. D., et al. 2014, [AJ](#), **147**, 37
- van Loon, J. T., Cioni, M.-R. L., Zijlstra, A. A., & Loup, C. 2005, [A&A](#), **438**, 273
- Weiler, K. W., Panagia, N., Stockdale, C., et al. 2011, [ApJ](#), **740**, 79
- Wellons, S., Soderberg, A. M., & Chevalier, R. A. 2012, [ApJ](#), **752**, 17
- Wheeler, J. C., Barker, E., Benjamin, R., et al. 1993, [ApJL](#), **417**, L71
- Wheeler, J. C., Harkness, R. P., Khokhlov, A. M., & Hoefflich, P. 1995, [PhR](#), **256**, 211
- Wheeler, J. C., Johnson, V., & Clocchiatti, A. 2015, [MNRAS](#), **450**, 1295
- Wheeler, J. C., & Levreault, R. 1985, [ApJL](#), **294**, L17
- Woosley, S., & Weaver, T. 1995, [ApJS](#), **101**, 181
- Yoon, S.-C., Woosley, S. E., & Langer, N. 2010, [ApJ](#), **725**, 940